THE JOURNAL OF PHYSICAL CHEMISTRY C
A JOURNAL OF THE AMERICAN CHEMICAL SOCIETY

pubs.acs.org/JPCC
Article

Tunable Generation of Reactive Oxygen Species in SnO_2/SnS_2 Nanostructures: Mechanistic Insights into Indigo Carmine Photodegradation

Kinga Michalec,* Bartosz Mozgawa,* Anna Kusior, Piotr Pietrzyk, Zbigniew Sojka, and Marta Radecka

Cite This: J. Phys. Chem. C 2024, 128, 5011−5029

Read Online

ACCESS | Metrics & More | Article Recommendations | Supporting Information

ABSTRACT: In semiconductor-based photocatalysis, one of the most significant directions in future research is designing materials with improved activity for the targeted photodegradation of organic contaminants. However, obtaining such photocatalysts requires an in-depth mechanistic understanding of the involved interfacial processes. In this framework, a comprehensive knowledge of photocatalysts' ability to produce particular reactive oxygen species (ROS) and their interaction with contaminants is particularly crucial. This work aims to examine how the phase composition of SnO_2/SnS_2-based nanomaterials (from bare SnO_2 to SnS_2) affects their ability to generate various ROS and propose the corresponding photodegradation mechanism. To this end, we combined three methods: scavenger tests, electron paramagnetic resonance (EPR) spin trapping techniques, and UV−vis nitro blue tetrazolium (NBT) assay. To demonstrate the implications of different ROS involved in the photodegradation of a particular substance, indigo carmine (IC) dye was chosen as a model contaminant. The second purpose of this study was to reveal and explain side effects that appear during tests with commonly applied scavengers. The results demonstrate the possibility of tunable ROS generation (from $^{\bullet}OH$ through $^1O_2$ to $O_2^{\bullet-}$) in SnO_2/SnS_2-based photocatalysts and the crucial role of superoxide radicals in the IC photodegradation. These findings were correlated with the band diagrams to rationalize the mechanisms of ROS formation and IC degradation. The applied experimental approach demonstrated the importance of using multiple techniques to examine ROS generation processes and elucidate their mechanistic roles.

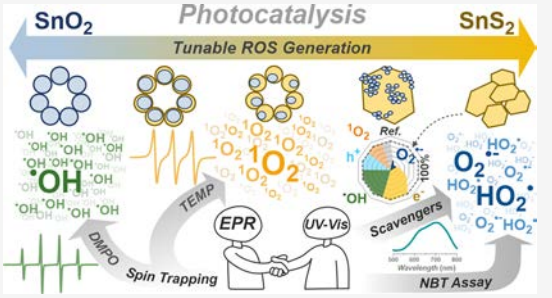

1. INTRODUCTION

In recent years, advanced oxidation processes (AOPs) have become one of the most investigated and intensively developing research areas for wastewater purification.[1−3] The fundamental principle of AOPs lies in generating highly active oxidizing agents, mainly reactive oxygen species (ROS), which can degrade (in)organic pollutants into harmless molecules.[1,4] Among various AOPs, semiconductor-based photocatalytic systems are believed to be a promising environmentally friendly technology for the future.[5] This is due to the possibility of using solar energy, operating under ambient pressure and temperature, high surface area of photocatalysts for redox reactions, reusability, and relatively low operating costs.[5,6]

To date, many strategies have been investigated to improve the photodegradation efficiency of pollutants, and they mainly involve modifying photocatalysts' properties or controlling reaction conditions.[3,5,7] However, the issue of selecting an appropriate photocatalyst for contaminant degradation is often neglected. The photodegradation mechanisms of different organic pollutants by ROS vary from each other.[8] Therefore, knowledge of ROS-contaminant interactions is essential to achieve high photodegradation performance. Similarly, it is also vital to study the photocatalysts' ability to generate specific reactive species on their surface.[8−10] Only merging both aspects will allow for an in-depth understanding of photodegradation mechanisms and, consequently, the conscious design of photocatalysts with high activity and selectivity.

Among ROS, we can distinguish four main types that can be generated via the interaction of photoinduced electrons (e^-) and holes (h^+) with oxygen or water molecules adsorbed on the photocatalyst's surface. These species include singlet oxygen ($^1O_2$), superoxide radical ($O_2^{\bullet-}$), hydrogen peroxide (H_2O_2), and hydroxyl radical ($^{\bullet}OH$).[10] The possible reactions of their formation, along with the corresponding redox potentials, are summarized in Table 1.

It is worth noting that in aqueous solutions, $O_2^{\bullet-}$ exists in a dynamic equilibrium with its protonated form—a hydro-

Received: December 14, 2023
Revised: February 25, 2024
Accepted: March 1, 2024
Published: March 14, 2024

https://doi.org/10.1021/acs.jpcc.3c08165
J. Phys. Chem. C 2024, 128, 5011−5029

Table 1. Selected Reactions for the Formation of the Most Important ROS Together with Their Reduction Potential Values[10,11]

ROS	reaction type	equation	eq no.	reduction potential, E vs NHE (pH = 7)/V
superoxide ($O_2^{\bullet-}$)/hydroperoxyl ($HO_2^{\bullet}$) radical	reduction	$e^- + O_2 \rightarrow O_2^{\bullet-}$	1	−0.16
		$e^- + O_2 + H^+ \rightarrow HO_2^{\bullet}$	2	−0.046[a]
		$e^- + {}^1O_2 \rightarrow O_2^{\bullet-}$	3	0.81
singlet oxygen ($^1O_2$)	oxidation	$h^+ + O_2^{\bullet-} \rightarrow {}^1O_2$	4	see reaction 3
hydrogen peroxide (H_2O_2)	reduction	$e^- + O_2^{\bullet-} + 2H^+ \rightarrow H_2O_2$	5	0.91
		$e^- + HO_2^{\bullet} + H^+ \rightarrow H_2O_2$	6	1.05
	oxidation	$2h^+ + 2H_2O \rightarrow H_2O_2 + 2H^+$	7	1.35
hydroxyl radical ($^{\bullet}OH$)	reduction	$e^- + H_2O_2 + H^+ \rightarrow {}^{\bullet}OH + H_2O$	8	0.39
		$e^- + H_2O_2 \rightarrow {}^{\bullet}OH + OH^-$	9	0.73
	oxidation	$h^+ + OH^- \rightarrow {}^{\bullet}OH$	10	1.97
		$h^+ + H_2O \rightarrow {}^{\bullet}OH + H^+$	11	2.31

[a] E^0, standard reduction potential.

peroxyl radical ($HO_2^{\bullet}$)—which can be described by the following equation:

$$O_2^{\bullet-} + H^+ \rightleftharpoons HO_2^{\bullet} \ (pK_a = 4.8) \quad (12)$$

The pK_a value of the above reaction indicates that at pH < 4.8, $HO_2^{\bullet}$ is the predominant form of this radical species.[10,12] Protonation of superoxide radicals may affect their reactivity with various molecules, as $O_2^{\bullet-}$ radicals are anions and $HO_2^{\bullet}$ radicals are uncharged species. $HO_2^{\bullet}$ radicals generally exhibit higher oxidizing ability than $O_2^{\bullet-}$.[13−15]

Overall, the occurrence of the ROS generation reactions collated in Table 1 depends on the position of the semiconductor's valence and conduction band edge energy levels (E_{VB} and E_{CB}, respectively) with respect to the ROS redox potentials (E_{redox}), namely $E_{VB} < E_{redox} < E_{CB}$.[5] However, if either of these conditions is not met, it does not necessarily mean that the particular ROS cannot exist in a given reaction system. Due to their high reactivity, ROS can be transformed into other species, for example, through recombination reactions.[10]

The complexity of ROS generation pathways makes it vital to experimentally ascertain their presence in analyzed photocatalytic systems and, consequently, to elucidate the photodegradation mechanism. To this end, one of the most commonly applied methods is photocatalytic tests in the presence of substances called scavengers (quenching tests).[16,17] In these experiments, the higher inhibition of a photodegradation reaction indicates the more significant role of the investigated ROS (or photogenerated charge carriers). However, the observed quenching effect is affected by many factors, such as the concentration of a scavenger or its interaction with molecules present in the solution.[16−19] Consequently, scavenger tests can lead to misleading conclusions.[16,17] Therefore, to reliably investigate the photodegradation mechanism, it is crucial to combine these tests with other techniques, such as electron paramagnetic resonance (EPR) in conjunction with spin trapping or UV−vis/fluorescence spectroscopy (by using suitable chemical probes).[10,12,16,17]

In this work, we have chosen to focus on SnO_2/SnS_2-based photocatalysts, heterostructures composed of wide (SnO_2, E_g = 3.5−3.8 eV[20−22]) and narrow bandgap (SnS_2, E_g = 2.0−2.4 eV[23−26]) semiconductors sharing the common tin(IV) cation. By combining the properties of SnO_2 and SnS_2, this system offers various advantages, such as an extended absorption range to visible light and an improved separation of photogenerated charge carriers.[27−29] SnO_2, due to its VB edge level (E_{VB} = 3.3−3.8 V vs NHE,[20,30] depending on pH), is often considered an oxidative photocatalyst. Thus, it can oxidize water molecules to form $^{\bullet}OH$ radicals. SnS_2, in turn, is regarded as a reductive photocatalyst ($E_{CB} \sim -0.5$ to −0.2 V vs NHE[23,25,28]) that generally can reduce oxygen molecules to $O_2^{\bullet-}$. Nevertheless, depending on the actual photocatalyst form and the applied process conditions, the VB and CB levels may shift, affecting the overall reactivity.[20,31,32]

Some recent studies[24,28,29] have included analysis of the dye/Cr(VI) photodegradation mechanism by selected SnO_2/SnS_2 composites. The idea of composition-directed ROS generation in semiconductor photocatalysts, in turn, has been introduced in the works of He et al.,[33,34] where bare ZnO and ZnS materials or mixed metal sulfides ($ZnIn_2S_4$, $CdIn_2S_4$, and $AgInS_2$) have been analyzed. However, to date, the possibility of composition-controlled tunable ROS generation in tin-based compounds (SnO_2, SnO_2/SnS_2, SnS_2) has not been investigated so far. Furthermore, to our best knowledge, the $^1O_2$ generation process in SnO_2/SnS_2 systems has also not been examined.

This work aims at establishing how the phase composition of SnO_2/SnS_2-based nanomaterials (ranging from bare SnO_2 through SnO_2/SnS_2 composites to SnS_2) affects their ability to generate specifically various ROS (especially $O_2^{\bullet-}$, $^{\bullet}OH$, and $^1O_2$) and proposing the associated photodegradation mechanism. To show the implications of different ROS involved in the photocatalytic degradation of a particular substance, we conducted research on the example of the indigo carmine (IC) dye. The presented study also discusses possible ROS formation mechanisms and their reactivities with organic species.

Moreover, as scavenger tests can lead to inconsistent conclusions about the photodegradation mechanism in various systems, our second aim was to show and discuss the observed side effects during tests with commonly applied scavengers. We believe that the presented work may be valuable for future interpretation of scavenger tests in various sulfide-based systems, which characterize lower stability than oxide materials. The conducted experiments were combined with EPR spin trapping analysis and UV−vis NBT (nitro blue tetrazolium) assay, which we adapted from biological systems to inorganic photocatalysts' investigations.

Thus, the novelty of this work is manifold: (1) it proposes the composition-controlled tunable ROS generation (from $^{\bullet}OH$ through $^1O_2$ to $O_2^{\bullet-}$) in SnO_2/SnS_2-based photo-

https://doi.org/10.1021/acs.jpcc.3c08165
J. Phys. Chem. C 2024, 128, 5011−5029

Table 2. Summary of Applied Methods for ROS/Charge Carriers Detection

	detected species			applied substance (scavenger/spin trap)	remarks
	symbol	name	method		
ROS	$O_2^{\bullet-}$	superoxide radical	scavenger tests	p-benzoquinone (pBQ)	tested concentration range[a]: 1−50 mM
			EPR	5,5-dimethyl-1-pyrroline N-oxide (DMPO)	1:1 (v/v) water−methanol solution
			NBT assay	nitro blue tetrazolium (NBT)	steps after illumination: -washing out unreacted NBT -NaOH solution and dimethyl sulfoxide (DMSO)
	$^{\bullet}OH$	hydroxyl radical	scavenger tests	*tert*-butyl alcohol (TBA)	tested concentration range[a]: 1:160 − 1:20 (v/v) TBA-water solution
			EPR	5,5-dimethyl-1-pyrroline N-oxide (DMPO)	aqueous solution
	$^1O_2$	singlet oxygen	scavenger tests	sodium azide (NaN_3)	tested concentration[a]: 10 mM
			EPR	2,2,6,6-tetramethylpiperidine (TEMP)	5:1 (v/v)acetonitrile-TEMP solution
	$SO_4^{\bullet-}$ and $^{\bullet}OH$	sulfate and hydroxyl radicals	scavenger tests	methanol (MeOH)	tested concentration range[a]: 10−100 mM
charge carriers	e^-	electron	scavenger tests	copper(II) nitrate ($Cu(NO_3)_2$) silver nitrate ($AgNO_3$) potassium dichromate ($K_2Cr_2O_7$) potassium persulfate ($K_2S_2O_8$)	tested concentration range[a]: 0.1−100 mM
	h^+	hole	scavenger tests	disodium ethylenediaminetetraacetate (EDTA-2Na)	tested concentration range[a]: 0.1−10 mM

[a]Concentration of a scavenger solution (1.5 mL), which was added to the IC aqueous solution (50 mL).

catalysts, (2) elucidates the possible side reactions of the analyzed catalytic materials with scavengers, and (3) combines the scavenger tests with both EPR spin trapping method and NBT assay for a more detailed analysis of such systems. Moreover, the presented study elucidates the mechanisms of ROS formation and the associated IC degradation process. The authors believe that this work can contribute to the rational design of promising photocatalysts for the efficient degradation of organic pollutants.

2. EXPERIMENTAL SECTION

2.1. Chemicals. All details on the chemicals used are presented in the Supporting Information (Text S1).

2.2. Synthesis. The synthesis procedure of SnO_2 and SnO_2/SnS_2 nanomaterials was described in our previous study.[35] Briefly, SnO_2 with "Raspberry-like Spheres" morphology (RS) was obtained by dissolving $Na_2SnO_3{\cdot}3H_2O$ (30 mmol) and glucose (120 mmol) in deionized water (200 mL). Subsequently, the mixture was placed in a Teflon-lined stainless-steel autoclave (BR-300, Berghof GmbH) and heated at 140 °C for 3 h. After centrifugation, washing in water/ethanol mixture (1:1 v/v), and drying, the powder was annealed in air at 500 °C for 3 h.

In the case of SnO_2/SnS_2 heterostructures, the typical experimental procedure involved the following steps: (1) the preparation of RS (1.6576 g) suspension in a solution of deionized water (180 mL) and HCl (10 mL); (2) the addition of a sulfide precursor (thioacetamide, TAA) in variable amounts; (3) hydrothermal treatment at 140 °C for 60 min; and (4) centrifugation, washing in water/ethanol mixture (1:1 v/v), and drying at 40 °C in a vacuum oven. Samples labeled RS_1:2, RS_1:1, and RS_2:1 were synthesized using the 1:2, 1:1, and 2:1 molar ratios of TAA to RS, respectively. Thus, in the case of RS_1:2, RS_1:1, and RS_2:1, 0.4132, 0.8265, and 1.6529 g of TAA were added to the RS suspension, respectively.

As applying more and more sulfide precursor (TAA) resulted in the formation of additional phases in the systems (sulfur and Sn_2OSO_4), bare SnS_2 (sample labeled SH − from "Sulfide with Hexagonal plate-like morphology") was synthesized via the same procedure as the RS_2:1 sample, with the difference that $SnCl_4{\cdot}5H_2O$ was used instead of the RS powder (as Sn(IV) precursor).

2.3. Materials Characterization. The characterization of (micro)structural, optical, surface, adsorptive, and photocatalytic properties of the SnO_2 (RS) and SnO_2/SnS_2 (RS_1:2, RS_1:1, and RS_2:1) samples was described in detail in our previous works.[35,36] The SnS_2 (SH) sample was characterized according to the same procedures (presented in the Supporting Information (Text S2)). Calculations of the materials' valence and conduction band edge levels (E_{VB} and E_{CB}, respectively) were performed by applying the atomic electronegativities-based method,[37] in which we used the bandgap (E_g) and isoelectric point (IEP) values determined experimentally in our previous works.[35,36] For the IC dye, the energies of HOMO and LUMO levels (the highest occupied and lowest unoccupied molecular orbitals, respectively) were established by applying cyclic voltammetry (CV) measurements with ferrocene (Fc) as an internal standard.[38,39] The HOMO−LUMO energy gap of the IC powder was determined by UV−vis total reflectance spectroscopy for comparison purposes. A detailed description of the experimental procedure is provided in the Supporting Information (Text S3).

2.4. Scavenger Tests. Photocatalytic tests with scavengers were performed in a cylindrical photoreactor that comprised 12 UV−vis Philips TL 8W/54−765 lamps (or UV TL 8W BLB mercury lamps for the SnO_2 sample). Typically, 62.5 mg of a photocatalyst was added to 50 mL of a 5×10^{-5} M IC solution in a quartz reaction vessel (beaker). Before illumination, the mixture was stirred magnetically for 30 min in the dark (to reach the equilibrium between the adsorption−desorption processes of dye molecules on the photocatalysts' surface).

https://doi.org/10.1021/acs.jpcc.3c08165
J. Phys. Chem. C 2024, 128, 5011−5029

Scheme 1. Summary of Methods for Presenting the Results of Scavenger Tests: (A) Photodegradation Kinetics, Which Includes Dye Adsorption after Stirring in the Bark, (B) Bar Charts, Which Compare Only the Quenching Effect under Illumination, and (C) Charts with Normalized Dye Degradation after 60 min, Where "100%" Indicates the Amount of Degraded Dye ($1 - C/C_0$) without Adding Any Scavenger

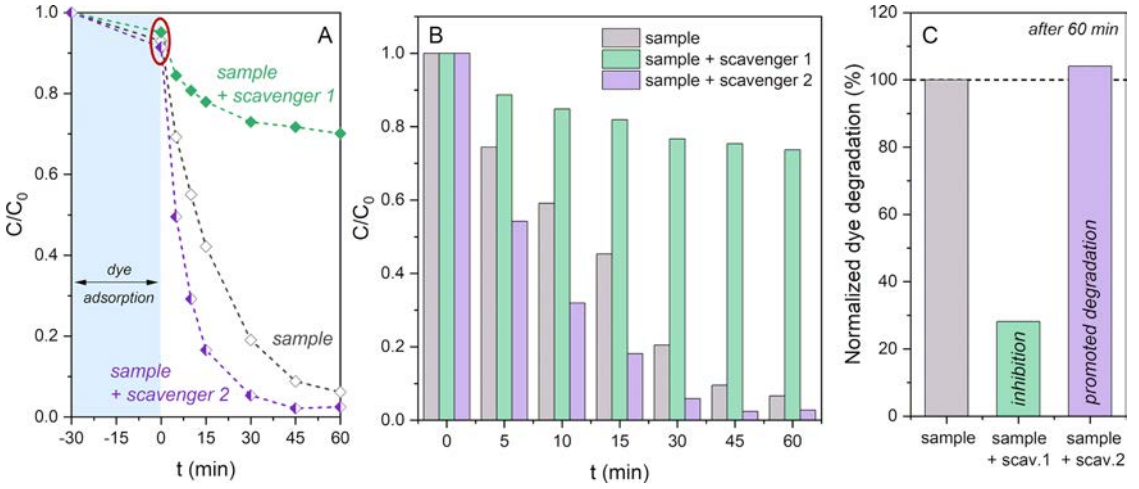

Subsequently, 1.5 mL of scavenger solution was added to the system. The mixture was stirred magnetically for 1 min and placed in the photoreactor. During the tests, the samples (3 mL) were collected through a syringe filter at specific time intervals and analyzed using a double-beam UV−vis−NIR V-670 spectrophotometer. The pH values of the IC-photocatalyst mixtures were not modified.

Scavenger concentrations were individually adjusted for each sample. The applied scavengers and their tested concentration ranges are summarized in Table 2. In general, the choice of concentrations was dictated by a compromise between the highest quenching effect and the lack of side effects, described in the Section 3. The performed experiments revealed that it was crucial to apply increasing scavenger concentrations as the SnS_2 content in the samples was higher (to observe the quenching effect without side effects). For example, in the case of p-benzoquinone (pBQ), concentrations of 10, 20, and 50 mM were selected for RS_1:1, RS_2:1, and SH, respectively (these concentrations refer to the volume of 1.5 mL of scavenger solution, which was added to 50 mL of the dye). The results showing the adjustment of scavenger concentrations are presented in the Supporting Information, while the selected concentrations for samples' comparison are described in the Section 3.

Relative concentrations (C/C_0) of IC solutions were calculated from changes in the absorbance intensity (A/A_0, where A_0 is the maximum absorbance of the reference sample). We chose three ways of presenting the results: (1) kinetics of the dye degradation—to show the effect of applied scavenger on dye adsorption—here as A_0 we assumed the absorbance of the scavenger-dye solution without photocatalyst (Scheme 1A); (2) bar charts—to compare only the quenching effect between the samples and nullify different initial adsorption (in some cases the samples adsorbed significantly different amounts of dye depending on the applied scavenger concentrations)—where we assumed as A_0 the absorbance of the powder-scavenger-dye mixture just before illumination (Scheme 1B); (3) normalized dye degradation after 60 min—to compare the quenching effect between different scavengers—for each sample, as "100%" we assumed the amount of degraded dye ($1 - C/C_0$) without adding any scavenger (Scheme 1C).

To analyze only the interactions of scavengers with the dye, we also performed illumination tests without photocatalysts (for each quenching agent). In these experiments, we used the highest concentrations tested for each scavenger, as listed in Table 2.

2.5. EPR Measurements. The Bruker ELEXSYS-E500 X-band spectrometer with a rectangular TE102 cavity that operates at 100 kHz field modulation was used to record the EPR spectra. Irradiation was conducted using a 50 W mercury lamp. For spin trapping measurements, typically, 2 mg of the sample was suspended in 0.5 mL of deionized water (or methanol), sonicated for 5 min, and mixed with 0.5 mL of DMPO (5,5-dimethyl-1-pyrroline N-oxide) solution (40 mg/10 mL). Singlet oxygen detection was performed by suspending and sonicating 2 mg of each sample in 0.5 mL of acetonitrile and 0.1 mL of TEMP (2,2,6,6-tetramethylpiperidine) solution. The obtained suspensions were transferred to a capillary and measured under illumination every 13 s for 10 min. All simulations and deconvolutions were carried out using EPRSim32 software.[40] The separated spectra were doubly integrated to attain quantitative information about the amounts of radicals generated in each experiment, yielding the relative intensities (the continuous wave EPR spectra are recorded in first derivative form). The EPR tests for $O_2^{\bullet-}$, $^{\bullet}OH$, and $^1O_2$ detection are summarized in Table 2.

2.6. NBT Assay. The UV−vis NBT assay for $O_2^{\bullet-}$ detection was carried out with a Cary 60 UV−vis spectrophotometer (Agilent Technologies). Typically, 2 mg of solid sample was suspended in 0.5 mL of deionized water and transferred quantitatively to a quartz fluorescence cuvette, diluted with H_2O to the total of 2.5 mL, and mixed with 0.5 mL of NBT solution in deionized water (5 mg/20 mL). The vessel was placed on a magnetic stirrer under white-light irradiation (10 W cool white LED with a color temperature between 6500 and 7000 K provided by Epistar) and measured at 0, 10, 20, and 30 min of illumination. Subsequently, the unreacted solution was washed several times with deionized water through sedimentation/decantation until the adsorption band of NBT at 260 nm disappeared. Afterward, to the

https://doi.org/10.1021/acs.jpcc.3c08165
J. Phys. Chem. C 2024, 128, 5011−5029

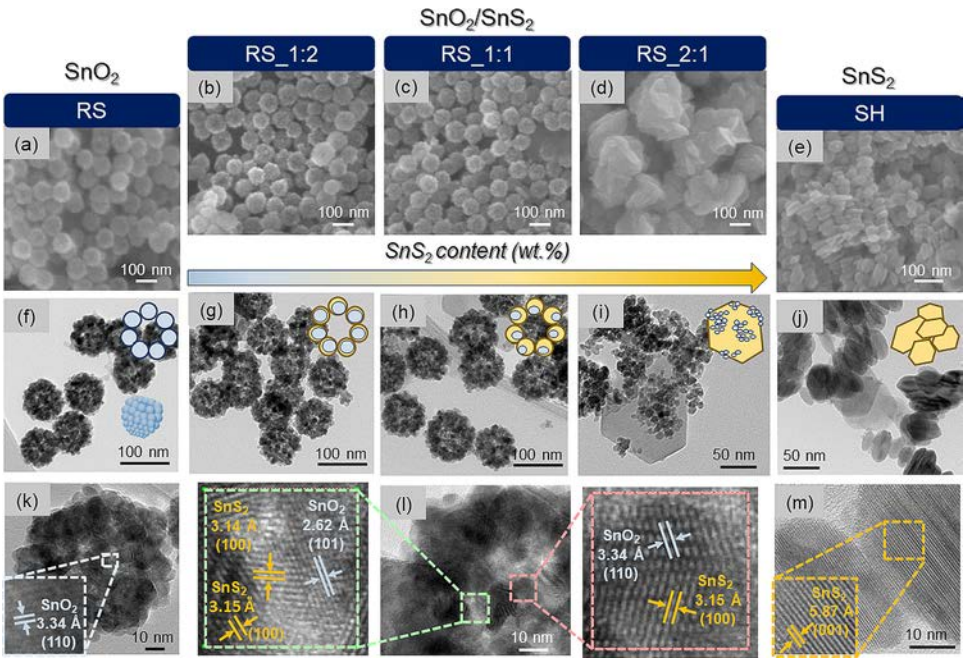

Figure 1. (a–e) SEM, (f–j) TEM, and (k–m) HR-TEM images with magnified areas obtained for the analyzed samples: (a, f, k) RS – SnO_2, (b, g) RS_1:2, (c, h, l) RS_1:1, (d, i) RS_2:1, and (e, j, m) SH – SnS_2. The determined *d*-spacing values and the corresponding crystallographic planes of SnO_2 or SnS_2 are marked in the magnified HR-TEM images.

Table 3. Selected Properties of the Samples

sample name	compound	phase composition (wt % SnS_2)[35]	TAA:Sn(IV) molar ratio	isoelectric point, IEP[36]	pH of IC + sample solution[a]	bandgap (eV)[35]		BET specific surface area (m^2/g)[35]
						SnO_2	SnS_2	
RS	SnO_2			4.61	8.7	3.72[b]		42.4
RS_1:2	SnO_2/SnS_2	2.6	1:2	4.47	4.1	3.89	2.41	51.2
RS_1:1		11.6	1:1	4.45	4.2	3.94	2.36	56.6
RS_2:1		32.9	2:1	4.24	4.1	[c]	2.25	59.9
SH	SnS_2	100	2:1	3.40	4.0		2.17	33.4

[a]The pH values of the IC-photocatalyst mixtures were not modified. [b]For RS, an additional optical transition with an energy of 3.27 eV (related to the presence of oxygen vacancies, V_O^{n+}) was detected.[35] [c]In the case of RS_2:1, the SnS_2 component masked the absorption edge of SnO_2 in the UV–vis spectrum.

remaining 0.5 mL of suspension, 0.5 mL of 2.5 M NaOH solution and 2 mL of DMSO (dimethyl sulfoxide) were added to dissolve the formazan obtained during the reduction of NBT with $O_2^{\bullet-}$. To estimate the adsorption of NBT on the surface of photocatalysts, we repeated an analogous procedure without illumination (to nullify the effect of superoxide formation). The NBT assay is briefly summarized in Table 2.

3. RESULTS AND DISCUSSION

3.1. Materials Characterization. The characterization of (micro)structural, optical, surface, adsorptive, and photocatalytic properties of SnO_2 (labeled RS – from "Raspberry-like Spheres") and SnO_2/SnS_2 heterostructures obtained via its chemical conversion (RS_1:2, RS_1:1, and RS_2:1, where 1:2, 1:1, and 2:1 represent sulfide precursor (TAA) to RS molar ratio) was described in detail in our previous studies.[35,36] Herein, we summarized their most significant properties and added characterization of bare SnS_2 (labeled SH – from "Sulfide with Hexagonal plate-like morphology") in Figure 1 and Table 3.

Briefly, the results revealed that applying a higher concentration of TAA during synthesis led to a higher SnS_2 content in the samples (see Table 3). However, too high TAA concentration also caused the formation of additional phases (RS_2:1 also contained S and Sn_2OSO_4 of 0.1 wt % in total) in the structures. Therefore, bare SnS_2 (SH sample) was obtained using $SnCl_4$ as a tin(IV) precursor (Table 3). Analysis of optical properties revealed that with increasing SnS_2 content in the samples, the bandgap related to SnO_2 increases, while this connected with the presence of SnS_2 decreases. This observation results from the decrease or increase in the particle size of SnO_2 or SnS_2, respectively. In the case of RS, an additional optical transition with an energy of 3.27 eV was detected. This transition is most likely related to the presence of oxygen vacancies in SnO_2-containing materials, which was documented in our previous work.[35] For RS_2:1, in turn, the SnS_2 component masked the absorption edge of the SnO_2 moiety in the UV–vis spectrum, which may be due to the covering of the SnO_2 surface by a thicker layer of SnS_2 (as compared to RS_1:2 and RS_1:1).[41]

Subsequently, previous analysis of the adsorptive properties[36] showed that the surface modification of SnO_2 with SnS_2 changes its affinity toward capture of the cationic/anionic dyes (RS showed enhanced adsorption of cationic rhodamine B, while the corresponding composites had greater affinity toward anionic IC). Based on the conducted experiments, IC was

https://doi.org/10.1021/acs.jpcc.3c08165
J. Phys. Chem. C 2024, 128, 5011–5029

chosen as a representative model dye for photocatalytic tests. These tests showed that increasing SnS_2 content in the samples improves the photodegradation rate of IC[36] (Figure 2).

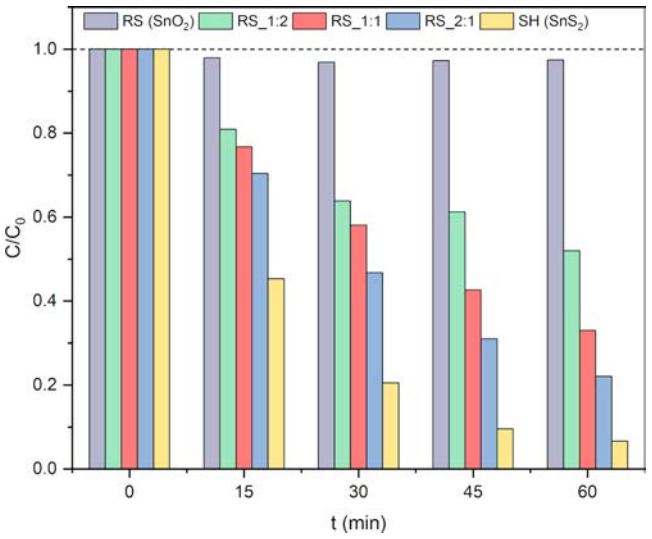

Figure 2. Photocatalytic activity of the investigated SnO_2, SnO_2/SnS_2, and SnS_2 materials in the IC degradation process.

However, depending on the degraded substance, the photocatalytic efficiency may change among the analyzed materials. This is related to the ROS and charge carriers (e^-, h^+) involved in the photodegradation mechanism. Therefore, to better understand the photocatalytic properties of SnO_2/SnS_2-based samples, it was crucial to examine first their ability to generate various reactive species in more detail.

3.2. Scavenger Tests. *3.2.1. IC–Scavenger Interactions.* Identification of ROS or charge carriers (e^-, h^+), which govern the photodegradation mechanism, is essential to assess the suitability of a material as a photocatalyst for a specific reaction.[16] One of the most common strategies for ROS detection is quenching tests, in which substances known as scavengers (see Table 2) are applied. However, the correct interpretation of these experiments requires a proper adjustment of the scavenger concentration to the examined reaction. Moreover, the scavenger itself should not react with a photocatalyst and should not decompose a dye under illumination.

Therefore, at the beginning, dye decomposition tests in the presence of the selected scavengers (without the photocatalysts) were carried out. The results are presented in Figure 3.

During 60 min of illumination, only silver nitrate ($AgNO_3$), commonly applied as an electron scavenger, significantly degraded IC (84% of the degraded dye). This can be related to the formation of metallic silver under light exposure:

$$nAg^+ + ne^- \xrightarrow{h\nu} Ag_n^0 \tag{13}$$

It has been reported that silver particles can decompose organic dyes, such as methyl orange or methylene blue.[42] This is also consistent with our observations (IC degradation). Another substance that caused partial decomposition of IC was $K_2S_2O_8$, also used as an e^- scavenger.[43] The peroxydisulfate ion ($S_2O_8^{2-}$) can undergo the following reactions:

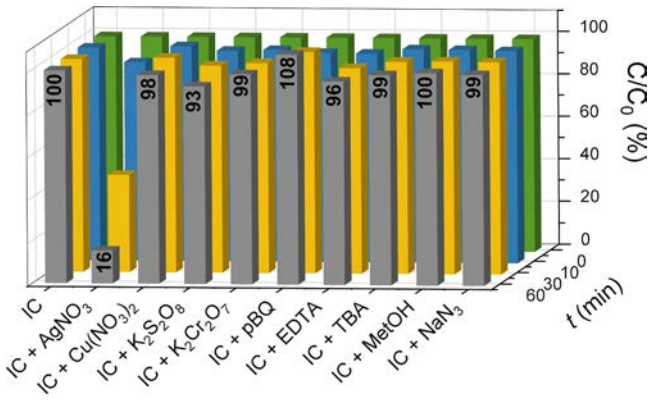

Figure 3. Blind tests performed under UV–vis illumination without any photocatalyst to assess the interactions of IC with the selected scavengers (C/C_0 – relative dye concentration).

$$S_2O_8^{2-} + e^- \rightarrow SO_4^{\bullet -} + SO_4^{2-} \tag{14}$$

$$SO_4^{\bullet -} + H_2O \rightarrow SO_4^{2-} + {}^{\bullet}OH + H^+ \tag{15}$$

Therefore, the resultant sulfate and hydroxide radicals ($SO_4^{\bullet -}$ and $^{\bullet}OH$, respectively) could contribute to the observed 7% dye degradation. In the case of p-benzoquinone (pBQ), which is the most frequently used superoxide radical ($O_2^{\bullet -}$) scavenger, the scavenging process is accompanied by direct interaction of pBQ with light. According to Fónagy et al.,[44] the photolysis route of pBQ depends on the pH and its concentration in the solution. For the analyzed conditions, this process may occur as follows:

$$\text{pBQ} \rightarrow {}^1(\text{pBQ})^* \rightarrow {}^3(\text{pBQ})^* \xrightarrow{+H_2O} \text{1,2,4-THB} \tag{16}$$

$$\text{1,2,4-THB} \xrightarrow{+O_2} \text{2-HO-BQ} \xrightarrow{+O_2} \text{2,5-HO-BQ} \tag{17}$$

$$\text{1,2,4-THB} + \text{pBQ} \rightarrow \text{2-HO-BQ} + H_2Q \tag{18}$$

Upon exposure to light, pBQ molecules are excited into the singlet state $^1(pBQ)^*$ and next undergo transformation into the triplet state $^3(pBQ)^*$. Subsequently, as a result of reactions with water, oxygen, and unreacted pBQ molecules (reactions 16–18), the following species are formed: 1,2,4-trihydroxybenzene (1,2,4-THB), 2-hydroxy-1,4-benzoquinone (2-HO-BQ), 2,5-dihydroxy-1,4-benzoquinone (2,5-HO-BQ), and hydroquinone (H_2Q). Consequently, due to the complex processes involving pBQ, IC may react with various intermediates present in the solution, leading to an apparent increase of the IC concentration to 108%. It remains in accordance with the blue shift of the IC absorbance maximum (cf. Figure S1a with Figure S1b in the Supporting Information). For the other tested scavengers (Figure 3), the IC concentration remained (slightly) unchanged (0–4%). It is also worth noting that IC itself is stable under illumination throughout the experiment time (0% of the degraded dye).

3.2.2. Photocatalyst–Scavenger Interactions. After examining scavenger–dye interactions, the next step was to adjust the scavenger concentration to the photocatalyst. Figure 4 shows the results obtained for pBQ. During the scavenging process, pBQ reacts with $O_2^{\bullet -}$, forming a p-benzosemiquinone radical anion ($BQ^{\bullet -}$). Subsequently, this radical undergoes transformation to hydroquinone (H_2Q), which is further degraded under aerobic conditions:[12,44,45]

https://doi.org/10.1021/acs.jpcc.3c08165
J. Phys. Chem. C 2024, 128, 5011–5029

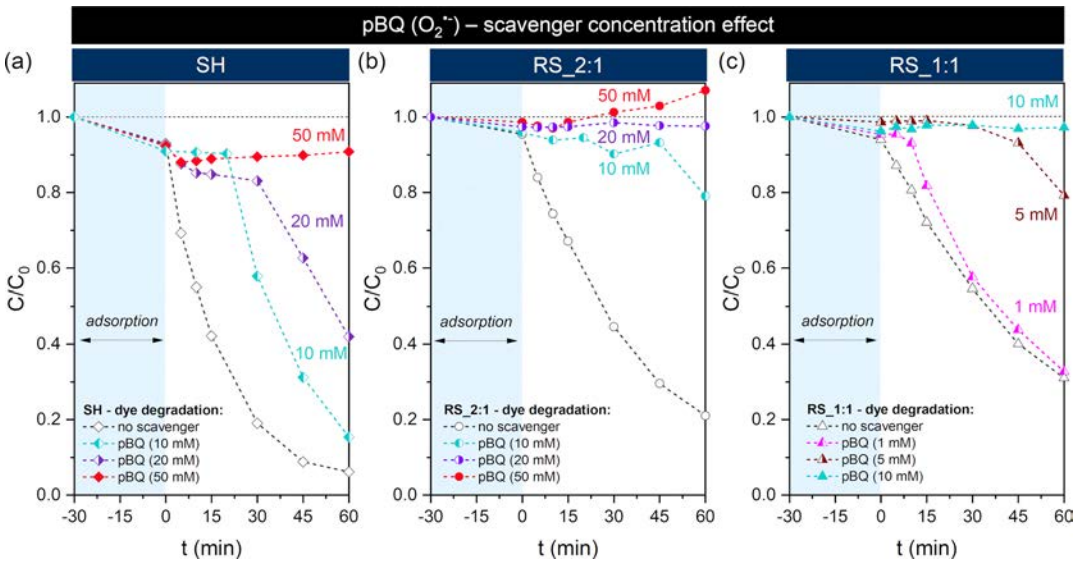

Figure 4. Effect of scavenger concentration (p-benzoquinone) on the observed quenching effect of IC degradation catalyzed by (a) SH, (b) RS_2:1, and (c) RS_1:1.

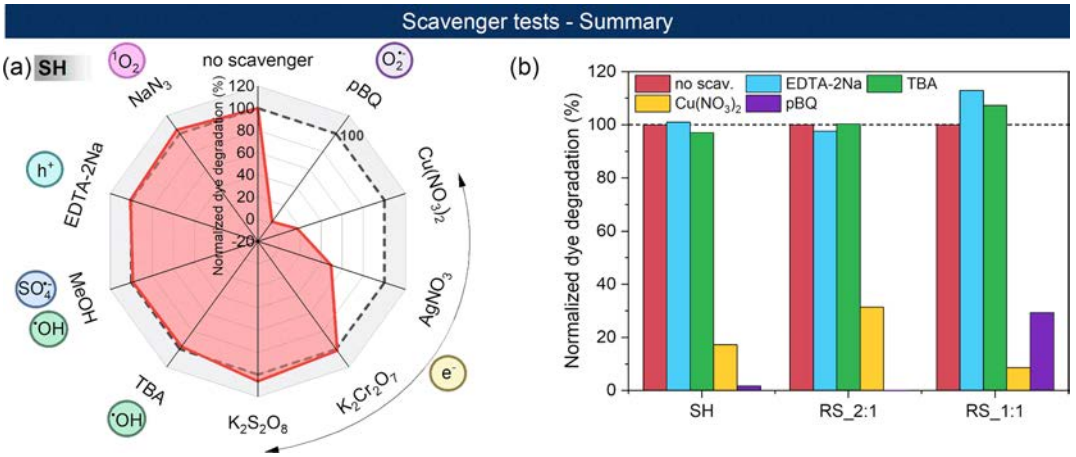

Figure 5. Summary of scavenger tests: (a) normalized dye degradation for SH (SnS_2) with added scavenger solutions (all tested scavengers), (b) comparison of the results obtained for SH, RS_2:1, and RS_1:1 with selected $O_2^{\bullet-}$, $^{\bullet}OH$, e^-, and h^+ scavengers. The following scavenger concentrations were used for SH, RS_2:1, and RS_1:1, respectively: pBQ − 50, 20, 5 mM; $Cu(NO_3)_2$ − 10, 1, 0.5 mM; TBA − 1:40, 1:80, 1:160 (v/v TBA-water solution); EDTA-2Na−1, 0.1, 0.1 mM. Additionally, for SH: $AgNO_3$ − 50 mM, $K_2Cr_2O_7$ − 10 mM, $K_2S_2O_8$ − 50 mM, MeOH − 10 mM, and NaN_3 − 10 mM.

$$\text{pBQ} + O_2^{\bullet-} \rightarrow \text{BQ}^{\bullet-} \xrightarrow{+2H^+} H_2Q \xrightarrow{+O_2^{\bullet-}} \text{aliphatic products} \quad (19)$$

Based on the obtained results, it can be concluded that (1) the proper adjustment of the pBQ concentration allows for almost complete inhibition of the dye degradation reaction, (2) the higher the SnS_2 content in the investigated sample (SH > RS_2:1 > RS_1:1), the higher pBQ concentration should be applied, and (3) $O_2^{\bullet-}$ radicals are generated throughout the whole process (e.g., 10 mM for SH − after initial inhibition of IC degradation, the dye started to decompose due to the insufficient amount of pBQ). However, in the case of excessive scavenger concentrations (e.g., 50 mM for RS_2:1), the effect of apparent "increasing" dye concentration is visible again (cf. Figure 3). Thus, the pBQ photolysis and/or other additional reactions with IC may overlap to some extent with the quenching effect.

The final concentrations of the individual scavengers were established based on the tests shown in Figure S2 (Supporting Information). Figure 5 summarizes these experiments for the SH, RS_2:1, and RS_1:1 samples. In the case of RS (SnO_2), no quenching tests were performed as its photocatalytic activity in the IC degradation was very low (less than 10% efficiency using UV lamps—see Figure S3 in the Supporting Information). According to our previous study,[36] this sample exhibits a negative surface charge in the IC solution. Thus, anionic IC molecules are not readily adsorbed on the surface of SnO_2. This fact, along with the wide bandgap value of SnO_2, could diminish IC photodegradation. For the remaining samples, as the SnS_2 content decreased (SH > RS_2:1 > RS_1:1 > RS_1:2), it was necessary to use more and more diluted scavenger solutions (even <0.1 mM). Therefore, the results for RS_1:2 are not presented in Figure 5. The selection of scavenger concentrations was dictated by maintaining a proper compromise between the highest quenching effect and the lack of side effects (such as the apparent "increasing" dye

https://doi.org/10.1021/acs.jpcc.3c08165
J. Phys. Chem. C 2024, 128, 5011−5029

concentration above 100%). The optimal values for each sample are included in Figure 5.

For the SH photocatalyst, the highest quenching effect was visible in the case of pBQ (Figure 5a). Therefore, it can be assumed that $O_2^{\bullet-}$ radicals play a crucial role in the IC decomposition (or decolorization) process. Based on these results, it can be expected that photogenerated electrons (involved in the formation of $O_2^{\bullet-}$ radicals) also play at least an indirect role in IC photodegradation. Interestingly, for substances known as e^- scavengers ($Cu(NO_3)_2$, $AgNO_3$, $K_2Cr_2O_7$, and $K_2S_2O_8$), two opposite sets of effects were observed. The addition of $Cu(NO_3)_2$ or $AgNO_3$ to the system resulted in significant inhibition of IC degradation, while the remaining ($K_2Cr_2O_7$, $K_2S_2O_8$) caused an acceleration of the photoreaction. The effect of promoted degradation in the case of $K_2S_2O_8$ may result from reactions 14 and 15. In the case of the $K_2Cr_2O_7$ scavenger, the scavenging process occurs according to the equation:

$$Cr_2O_7^{2-} + 6e^- + 14H^+ \rightarrow 2Cr^{3+} + 7H_2O \quad (20)$$

One possible explanation of the promoted dye degradation is the electrostatic repulsion between $Cr_2O_7^{2-}$ ions and IC (anionic dye). As a result of this phenomenon, dichromate anions might push IC molecules into the Stern layer of SH, improving the charge transfer between the dye and the photocatalyst. Consequently, the IC molecules were degraded more efficiently. This explanation is consistent with dye adsorption studies. Based on the kinetic curves shown in Figure S4a (Supporting Information), it can be observed that adding $K_2Cr_2O_7$ (10 mM solution) into the reaction system resulted in increased dye adsorption from 7 to 18%. Moreover, $O_2^{\bullet-}$ radicals have been reported to participate in reducing the Cr(VI) to Cr(III).[46] As these radicals are abundantly generated in SH-based systems, $K_2Cr_2O_7$ was also excluded from further analysis as the electron scavenger.

In the case of silver nitrate ($AgNO_3$), the dye underwent degradation without any photocatalyst (Figure 3). The addition of SH to the reaction mixture, in turn, resulted in a significant inhibition of dye degradation (Figure 5a). Therefore, this test may suggest that photogenerated electrons also participate in the reaction. However, metallic silver formed under irradiation (reaction 13) can be deposited on the photocatalyst surface, altering its photocatalytic properties.[43] Another possible side reaction is the formation of black-colored silver sulfide (Ag_2S) via in situ ion exchange.[47] In the case of the investigated system, adding the $AgNO_3$ solution resulted in the immediate precipitation of a black powder. Due to the interaction of this scavenger with both IC and the photocatalyst, we also excluded $AgNO_3$ from further analysis and confined further study to $Cu(NO_3)_2$ only. In the latter case, XRD analysis revealed that the phase composition of the SH powder remained unchanged after quenching tests (Figure S5).

Applying MeOH and TBA resulted in a slight inhibition of the studied reaction (1 and 3%, respectively). The former is known as a quenching agent for both hydroxyl ($^\bullet OH$) and sulfate ($SO_4^{\bullet-}$) radicals, while the latter is commonly applied as a hydroxyl radical scavenger due to its much higher affinity toward $^\bullet OH$ than $SO_4^{\bullet-}$. Therefore, the use of both scavengers can indirectly evaluate the contribution of $SO_4^{\bullet-}$ radicals to the degradation reaction.[16] Based on the obtained results, however, it can be assumed that only hydroxyl radicals participate in the IC decomposition, yet their contribution is almost insignificant. It is worth noting that both MeOH and TBA preferentially react with radicals present in the bulk solution.[16] Therefore, the role of $^\bullet OH$ radicals may be underestimated in these tests. Another aspect to consider is the reaction of methanol 21 or TBA 22 with hydroxyl radicals:

$$CH_3OH + {}^\bullet OH \rightarrow {}^\bullet CH_2OH + H_2O \quad (21)$$

$$(CH_3)_3COH + {}^\bullet OH \rightarrow {}^\bullet CH_2C(CH_3)_2OH + H_2O \quad (22)$$

During the scavenging processes, hydroxymethyl ($^\bullet CH_2OH$) and 2-hydroxy-2-methyl-1-propyl ($^\bullet CH_2C(CH_3)_2OH$) radicals are formed.[19,48,49] In general, hydroxyalkyl radicals ($^\bullet CH_2OH$, $^\bullet CH(OH)CH_3$, $^\bullet C(OH)(CH_3)_2$, etc.) are known as strong reducing agents (e.g., the redox potential of $^\bullet CH_2OH$ to formaldehyde is in the range of −0.9 to −1.18 V vs NHE).[49,50] Therefore, it is possible that these radicals can also participate in the IC degradation, resulting in an initially accelerated reaction (see Figure S4d in the Supporting Information).

In the case of EDTA-2Na acting as a h^+ scavenger, regardless of its concentration (see Figure S2g in the Supporting Information), only a slight quenching effect was observed at the beginning of the experiment (up to 15 min). After 60 min (Figure 5a), the efficiency of the process was almost unchanged (101% of normalized dye degradation). As photogenerated holes participate in generating $^\bullet OH$ radicals, their contribution to the IC degradation was expected to be insignificant.

The addition of NaN_3 ($^1O_2$ scavenger) to the reaction system, in turn, promoted dye degradation throughout the whole experiment (Figure S4e). According to Schneider et al.,[18] the reaction of azide anions with singlet oxygen may occur as follows:

$$N_3^- + {}^1O_2 \rightarrow N_3^\bullet + O_2^{\bullet-} \quad (23)$$

Thus, superoxide radicals ($O_2^{\bullet-}$), which play a crucial role in IC degradation, are formed, which explains the accelerated reaction. Moreover, azide radicals ($N_3^\bullet$) have also been reported to oxidize aromatic compounds via direct electron transfer.[18] Finally, azide anions may react with other ROS (e.g., $^\bullet OH$) in the following way:

$$N_3^- + {}^\bullet OH + H^+ \rightarrow N_3^\bullet + H_2O \quad (24)$$

Due to the side effects mentioned above, as well as the nonselectivity of NaN_3 toward singlet oxygen, this scavenger was excluded from further investigations.

Figure 5b summarizes the results obtained for the selected e^-, h^+, $O_2^{\bullet-}$, and $^\bullet OH$ scavengers. It can be noticed that regardless of the applied photocatalyst, the trend is the same. The species that are primarily responsible for the IC degradation are superoxide radicals ($O_2^{\bullet-}$) and electrons (e^-), while the role of hydroxyl radicals ($^\bullet OH$) and holes (h^+) is minor. However, the scavenger tests suggest that increasing the SnO_2 content in the samples alters the photodegradation mechanism. In the case of RS_1:1, applying TBA and EDTA-2Na resulted in a significant acceleration of the IC photodecomposition reaction (107 and 113% of the normalized dye degradation, respectively). For SH and RS_2:1, in turn, almost no changes were observed. In addition, the scavenger tests did not allow for the unambiguous analysis of RS and RS_1:2. Therefore, to investigate the effect of phase composition on the photocatalytic properties of the samples, it was crucial to apply additional spectroscopic techniques.

https://doi.org/10.1021/acs.jpcc.3c08165
J. Phys. Chem. C 2024, 128, 5011−5029

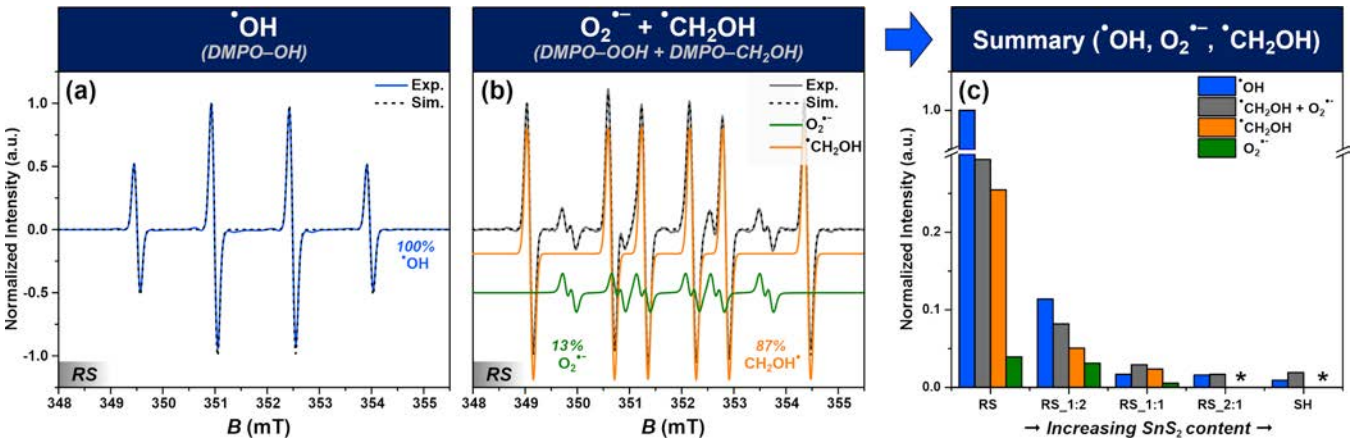

Figure 6. (a, b) EPR spectra of photogenerated radicals trapped with DMPO over the RS (SnO_2) sample in (a) aqueous and (b) 1:1 (v/v) water−methanol solution; (c) double integrated intensities of DMPO-based radical adducts formed during illumination of the samples. Separation of the $^{\bullet}CH_2OH$ and $O_2^{\bullet-}$ components was carried out based on computer simulations of the recorded EPR spectra (*the samples where the EPR intensities were too low for accurate deconvolution).

3.3. EPR Measurements. *3.3.1. Hydroxyl Radical Detection.* To complement the results of the scavenger tests and establish the nature of active species involved in the IC degradation catalyzed by SnO_2/SnS_2 photocatalytic materials, a series of EPR spin trapping experiments were carried out. For this purpose, 5,5-dimethyl-1-pyrroline N-oxide (DMPO) was used to detect hydroxyl ($^{\bullet}OH$) and superoxide ($O_2^{\bullet-}$) radicals.[18,51] Due to the equilibrium between $O_2^{\bullet-}$ and its protonated form ($HO_2^{\bullet}$) in aqueous solutions (reaction 12), signals from both DMPO-O_2^- and DMPO-OOH adducts can be expected. However, in solvents such as water or methanol, the latter is predominantly detected due to the protic nature of such environments.[52] Note that if both $O_2^{\bullet-}/HO_2^{\bullet}$ and hydroxyl ($^{\bullet}OH$) radicals are produced simultaneously in an aqueous solution under irradiation, direct detection of DMPO-OOH adduct may be impossible.[18] This is due to the much higher rate constant for the reaction between DMPO and $^{\bullet}OH$ ($k = 3.4 \times 10^9$ M^{-1} s^{-1})[52] than DMPO and $O_2^{\bullet-}/HO_2^{\bullet}$ ($k = 1 \times 10^1$ or 6.6×10^3 M^{-1} s^{-1}, respectively)[53] in water. Thus, two parallel tests were carried out—one in aqueous solutions and the other in a 1:1 (v/v) water−methanol mixture. As shown in the previous section, methanol acts as the $^{\bullet}OH$ scavenger. Therefore, its addition can either divert the mechanism toward $O_2^{\bullet-}$ production (or its protonated form) or prevent the cross-reaction between the generated $^{\bullet}OH$ and $O_2^{\bullet-}$ radicals. However, in any case, the addition of hydroxyl scavenging CH_3OH (MeOH) species results in the formation of hydroxymethyl radicals ($^{\bullet}CH_2OH$)[54] (reaction 21). These radicals are also trapped by DMPO, forming a paramagnetic DMPO−CH_2OH adduct. An example of EPR spectra obtained for the RS (SnO_2) sample irradiated with and without MeOH, along with their simulations and deconvolution, is shown in Figure 6a,b.

Upon illumination of RS in the aqueous medium, a characteristic quartet signal centered at $g = 2.0054$ with an intensity ratio of 1:2:2:1 was observed (Figure 6a), which originates from DMPO−OH adducts ($^{\bullet}OH$ trapped by DMPO).[16] The characteristic hyperfine splitting pattern results from the coupling of the unpaired electron with the ^{14}N and ^{1}H nuclei ($A_N = 1.496$ mT, $A_H = 1.472$ mT). When methanol is introduced into the solution (Figure 6b), a distinct signal appears instead of the previously observed $^{\bullet}OH$ adducts. Computer simulation of this spectrum revealed that it can be decomposed into two separate signals originating from the DMPO-OOH[52] ($A_N = 1.418$ mT, $A_{H1} = 0.942$ mT, $A_{H2} = 0.150$ mT) and the DMPO−CH_2OH adducts[55,56] ($A_N = 1.560$ mT, $A_{H1} = 2.197$ mT).

When investigating the kinetic profiles of radical generation (Figure S6a in the Supporting Information) for RS, it can be noticed that after around 100 s of illumination, the intensity of the superoxide-DMPO adducts reaches a constant value. This implies the existence of a steady-state equilibrium that arises when $O_2^{\bullet-}$ radicals are generated and consumed at comparable rates. These results can be interpreted assuming that $^{\bullet}OH$ species are generated in a two-step reaction, where the superoxide radicals are first formed and then transformed into hydroxyl radicals. In the presence of a scavenger such as MeOH, the latter stage ($^{\bullet}OH$ generation) is disrupted, uncovering the intermediate step of $O_2^{\bullet-}$ formation. Without methanol, in turn, either the equilibrium can be significantly shifted toward the $^{\bullet}OH$ formation or some parallel recombination reactions may occur (e.g., Reaction S1 in Text S4). However, the relatively slow kinetics of DMPO-OOH formation and its instability in water (compared to DMPO−OH adduct) do not allow for determining which pathway predominates in an aqueous solution (without MeOH). The process of $^{\bullet}OH$ formation in RS can be complex. On the one hand, according to the literature,[27,57] photogenerated holes (h^+) in the valence band (VB) of SnO_2 possess a strong oxidizing ability (the VB edge level at E_{VB} = 3.3−3.8 V vs NHE[20,30]). Therefore, they can readily oxidize hydroxyl ions (OH^-) or water molecules to form $^{\bullet}OH$ radicals (the corresponding redox potential E = 1.9−2.7 V vs NHE, depending on the solution pH[16]). These processes can be described by reactions 10 and 11 in Table 1. On the other hand, SnO_2 is generally reported to exhibit the conduction band (CB) edge level insufficient to reduce molecular oxygen (O_2) by photogenerated electrons (reaction 1).[58−60] However, depending on the actual SnO_2 form and applied process conditions (e.g., solution pH), this level can shift toward the values that allow $O_2 \rightarrow O_2^{\bullet-}$ transformation.[61−63] Therefore, the $^{\bullet}OH$ radicals can also be generated through a two-step process, which involves $O_2^{\bullet-} \rightarrow H_2O_2$ reduction and the subsequent transformation of the intermediate product into

https://doi.org/10.1021/acs.jpcc.3c08165
J. Phys. Chem. C 2024, 128, 5011−5029

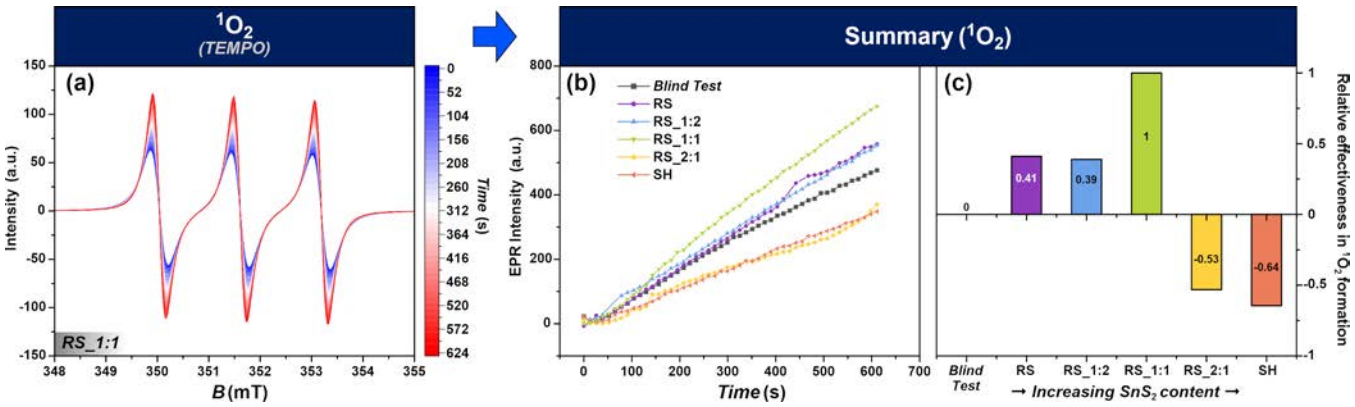

Figure 7. (a) EPR spectra of TEMP oxidation using photogenerated singlet oxygen over the RS_1:1 sample, (b) kinetic plots of TEMP oxidation over the analyzed samples, and (c) relative effectiveness of $^1O_2$ formation.

$^{\bullet}OH$ (reactions 5 and 9, respectively).[10,64] A more detailed discussion of the possible reaction mechanisms is provided below in the Section 3.5.2. Based on the performed investigations, it can be assumed that hydroxyl radicals ($^{\bullet}OH$) in the case of RS (SnO_2) are generated both by oxidation of OH^-/water (reactions 10 and 11) and conversion of $O_2^{\bullet-}$ radicals (reactions 5 and 9).

Analogous investigations using DMPO as a spin trap in either aqueous or water−methanol medium were repeated for all prepared samples (see Figure S7 in the Supporting Information), and the recorded spectra were simulated and decomposed into component signals (Figures 6 and S8). The histogram of their integral intensities is shown in Figure 6c, whereas the corresponding values are compiled in Table S1 (Supporting Information). The results reveal a clear correlation between the SnO_2 content in the samples and the formation of $^{\bullet}OH$ radicals. Namely, SnO_2 is much more beneficial for hydroxyl radical formation than bare SnS_2 or SnO_2/SnS_2 composites. However, the EPR method cannot accurately estimate the amounts of generated $O_2^{\bullet-}$ radicals, as applied solvents and experimental conditions strongly affect the obtained signals.[52] Therefore, only the data for $^{\bullet}OH$ radicals can be compared directly since the exact kinetics of the initial $O_2^{\bullet-}$ formation and the subsequent scavenging of $^{\bullet}OH$ with methanol are not precisely known. Based solely on the EPR experiments with DMPO, it could seem that SH (SnS_2) exhibits the lowest ability to generate $O_2^{\bullet-}$ radicals. However, the scavenger tests (see previous section) proved that with an increasing SnS_2 content in the samples, $O_2^{\bullet-}$ species are produced more abundantly. Therefore, the DMPO test was used to assess the efficiency of the $^{\bullet}OH$ radical generation among the analyzed materials and to gain some insight into the possible mechanism of its formation. Due to the limitations of the EPR method and scavenger tests, we proposed an additional method (see Section 3.4 below) to investigate the efficiency of $O_2^{\bullet-}$ generation for all samples (also RS and RS_1:2).

In summary, DMPO-based EPR measurements revealed that increased SnO_2 content in the samples improves their ability to generate $^{\bullet}OH$ radicals. These species may be formed: (1) directly by the reaction of photogenerated holes (h^+) in the VB of SnO_2 with OH^- ions/H_2O molecules or (2) via the conversion of $O_2^{\bullet-}$ radicals. Both reactions may proceed simultaneously. The proposed second mechanism is also consistent with the results of the scavenger tests. In the case of the SH sample, which is characterized by the highest capacity for the production of $O_2^{\bullet-}$ radicals, tests with TBA ($^{\bullet}OH$ scavenger) showed the most pronounced quenching effect among the tested samples (SH, RS_2:1, and RS_1:1). According to the literature[23] and our studies (see the Section 3.5.2 below), the VB edge of SnS_2 does not allow for direct generation of $^{\bullet}OH$ via the reaction with h^+. Therefore, scavenger tests (as well as EPR measurements) suggest that the $O_2^{\bullet-}$ → $^{\bullet}OH$ conversion also occurs in the investigated systems.

3.3.2. Singlet Oxygen Detection. In addition to the identified radicals, illumination of the examined photocatalytic materials can lead to the formation of other ROS. One of the most prevalent among them is singlet oxygen ($^1O_2$), which can contribute to the oxidation of organic compounds on the photocatalysts' surface.[65,66] This species can be formed via (1) energy transfer from the excited dye molecules to molecular oxygen in the triplet ground state ($^3O_2$) or (2) oxidation of superoxide radicals ($O_2^{\bullet-}$) by photogenerated holes (reaction 4 in Table 1), $HO_2^{\bullet}$ (Text S4, Reaction S2) or $^{\bullet}OH$[10] species (discussed in the Section 3.5.2 below). Since singlet oxygen may be generated via various pathways, its presence could not be excluded in the analyzed photocatalytic systems. As scavenger tests with sodium azide (NaN_3) could not give an unambiguous answer regarding the generation of $^1O_2$, applying an additional technique was crucial. $^1O_2$ is a singlet, thus not a paramagnetic species, and it cannot be observed directly using EPR spectroscopy. However, through a reaction with 2,2,6,6-tetramethylpiperidine (TEMP), it can form a relatively stable radical 2,2,6,6-tetramethyl-1-piperidinyloxy (TEMPO), which is observable in EPR. An example of such spectra is presented in Figure 7a.

The EPR signal of TEMPO (Figures 7a and S9) is a triplet (g = 2.0059) with relative intensities of 1:1:1 originating from hyperfine splitting due to the ^{14}N nucleus (A_N = 1.576 mT). It is crucial to notice that there is a nonzero intensity of TEMPO even under the "dark" condition (without illumination). This is related to the fact that commercially available TEMP samples all contain impurities of the oxidized TEMPO. However, the initial intensity of the EPR signal can easily be subtracted from the investigated spectra for proper extraction of the corresponding kinetic data in Figure 7b,c.

The collected spectra for all the analyzed samples (Figure S9 in the Supporting Information) were doubly integrated and plotted against time in Figure 7b and fitted to linear functions (Figure S10). The respective slope values were normalized and

https://doi.org/10.1021/acs.jpcc.3c08165
J. Phys. Chem. C 2024, 128, 5011−5029

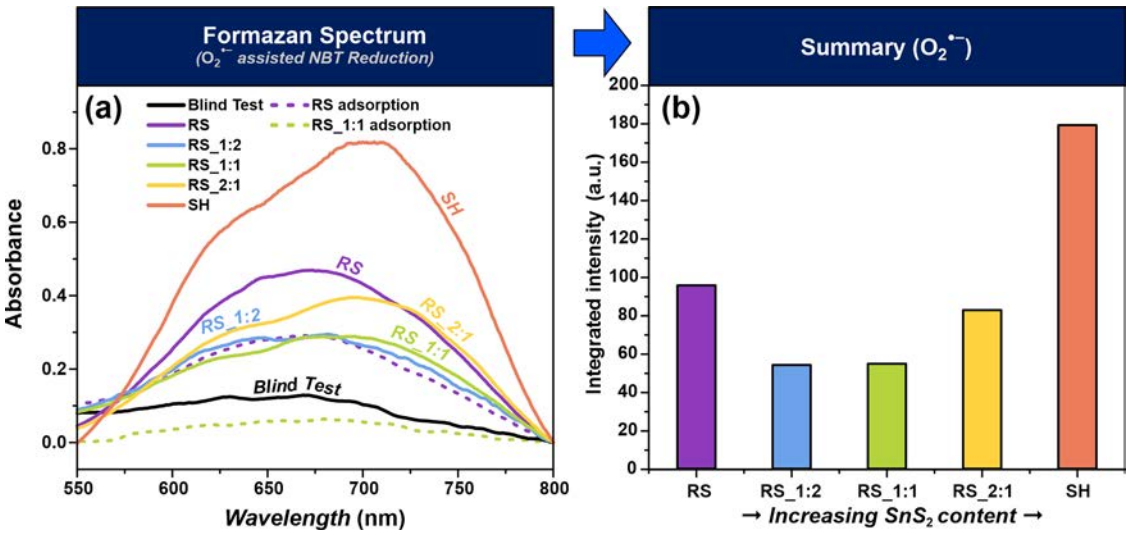

Figure 8. (a) Spectra of formazan formed during $O_2^{\bullet-}$-based reduction of NBT and (b) relative yield of $O_2^{\bullet-}$ formation.

shown in Figure 7c. The relative scale was set to "0" for the reaction rate of the blind sample (without any photocatalyst) and to "1" for the rate of the most active photocatalyst (RS_1:1). It is important to note that illumination with mercury arc lamp results in partial oxidation of TEMP to TEMPO. The substrate for the singlet oxygen formation can be molecular oxygen ($^3O_2$) dissolved in acetonitrile.[67] Therefore, for samples containing the highest SnS_2 content (RS_2:1 and SH), the effectiveness of $^1O_2$ generation is noticeably below the assumed "baseline." It is plausible that in this test, oxygen molecules can also be reduced to form $O_2^{\bullet-}$ species (reaction 1 in Table 1). It has been reported[68−70] that superoxide radicals may participate in TEMPO reduction, which can be responsible for the decay of the recorded EPR signal. With this in mind, the negative relative effectiveness of high-sulfide-containing samples (RS_2:1 and SH) may be attributed to changes in the mechanistic pathway from singlet oxygen ($^1O_2$) to superoxide radical ($O_2^{\bullet-}$) involvement. This is consistent with the scavenger tests (Figure 4, tests with pBQ), which also revealed the highest efficiency of $O_2^{\bullet-}$ generation for the samples with the highest SnS_2 content. Furthermore, in the case of SH, the test with sodium azide (Figures 5a and S4e) implies an enhanced $O_2^{\bullet-}$ generation (improved photodegradation efficiency) in the presence of the $^1O_2$ scavenger (reaction 23).

To sum up, the results of the TEMP-based EPR measurements revealed the highest ability to singlet oxygen generation for RS_1:1. Additionally, in the case of the samples with higher SnS_2 content (RS_2:1 and SH), a change in the mechanism pathway toward predominant $O_2^{\bullet-}$ generation was observed.

3.4. NBT Assay for Superoxide Radical Detection. Due to the limitations of scavenger and EPR tests in detecting superoxide radicals ($O_2^{\bullet-}$), a more targeted method had to be employed. Therefore, an NBT test, which is a characteristic solely for $O_2^{\bullet-}$ radicals, was carried out. This procedure, commonly used in various biological systems,[12,71] was successfully adapted for probing the superoxide species in the analyzed inorganic photocatalysts (see Figure S11 in the Supporting Information). The underlying assumption underneath the NBT assay lies in the selective reduction of this yellow-colored compound with superoxide radicals to form an insoluble in water formazan, which can then be dissolved using a basic solution (NaOH) and dimethyl sulfoxide (DMSO). This results in the formation of a teal-blue solution that can be measured using UV−vis spectroscopy. However, before this step, it is crucial to remove all excess (unreacted) NBT by washing with water, as it also produces a colored compound in the basic/DMSO solution, obscuring the $O_2^{\bullet-}$ quantification. Furthermore, for the investigated inorganic powder-suspension systems, it was necessary to check the effect of NBT adsorption on the photocatalysts' surface (since the adsorbed dye is dissolved upon treatment with NaOH/DMSO). The final spectra of formazan formed via $O_2^{\bullet-}$ reduction of NBT are depicted in Figure 8.

As expected, SH (SnS_2) turned out to be the most active photocatalyst in $O_2^{\bullet-}$ generation. Based solely on the absorbance spectra obtained for tests under illumination, it may apparently seem that RS (SnO_2) also exhibits significant activity. However, when the same procedure was repeated without illumination (to estimate the effect of dye adsorption on the photocatalysts' surface), it turned out that the RS sample adsorbed a considerable amount of NBT compared to the other samples (cf. the adsorption for RS with RS_1:1, represented by violet and green dashed lines in Figure 8a, respectively). The observed effect of pronounced NBT adsorption on the SnO_2 surface is consistent with our previous study,[36] which revealed that the bare SnO_2- and SnS_2-coated samples exhibit different adsorption properties. It turned out that the RS sample more favorably adsorbs cationic dyes, such as rhodamine B (NBT is also a cationic dye). The composites, in turn, show a higher affinity toward anionic indigo carmine adsorption.

Based on the obtained spectra under illumination, the efficiency of the $O_2^{\bullet-}$ formation was compiled in Figure 8b. It is evident that SH (SnS_2) has the highest activity toward $O_2^{\bullet-}$ generation, followed by the most sulfur-abundant composite (RS_2:1). This remains consistent with the results of singlet oxygen generation (see Section 3.3.2 above) and confirms the competition between the selectivity toward the $O_2^{\bullet-}$ and $^1O_2$ formation. For this reason, the RS_1:1 sample, which was the most active in $^1O_2$ generation according to the TEMP-based EPR tests, shows relatively the lowest production of superoxide radicals. Finally, NBT assay results prove that spin trapping of $O_2^{\bullet-}$ with DMPO does not produce accurate results in

https://doi.org/10.1021/acs.jpcc.3c08165
J. Phys. Chem. C 2024, 128, 5011−5029

aqueous media, in contrast to trapping of hydroxyl radicals (see Section 3.3.1 above).

3.5. Structure vs Photodegradation Mechanism.

3.5.1. Summary of Measurements. As scavenger tests could only provide qualitative information on the photocatalysts' capabilities to generate various ROS, the more quantitative EPR and NBT assay experiments were used for comparison purposes. The results concerning the $^{\bullet}OH$, $^{1}O_2$, and $O_2^{\bullet-}$ generation are shown in Figure 9.

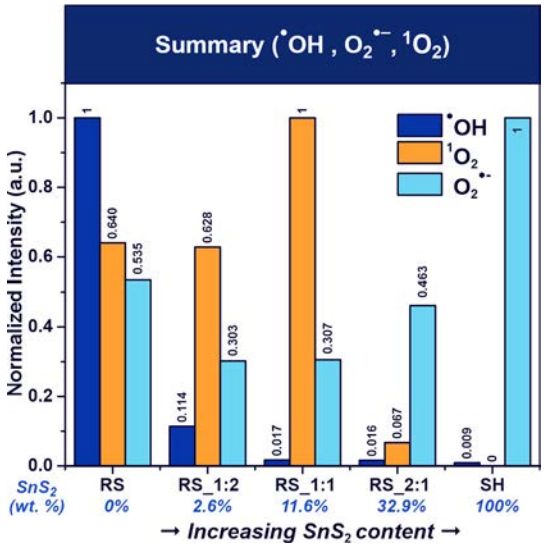

Figure 9. Overall activity of the analyzed SnO_2, SnO_2/SnS_2, and SnS_2 samples in ROS generation.

Based on the observed reactivity patterns, it was possible to establish a relative efficiency of generating different ROS over tin(IV) oxides/sulfides for the photocatalytic oxidation/reduction processes. Among all samples, bare SnO_2 (RS) is the most active in the formation of $^{\bullet}OH$ radicals. Its activity is nearly 10 times higher compared to even the lowest sulfide-containing sample (RS_1:2, with 2.6 wt % of SnS_2). This suggests that for the desired $^{\bullet}OH$-based photocatalytic processes, it would be beneficial to use the catalyst with an exposed SnO_2 layer on its surface.

With an increase in the SnS_2 content, we can observe a narrow composition range where $^{1}O_2$ is generated predominantly. The highest efficiency of singlet oxygen generation exhibits the RS_1:1 sample (11.6 wt % of SnS_2), which is most likely due to the interaction of hydroxyl and superoxide radicals generated over the SnO_2 and SnS_2 components, respectively:

$$O_2^{\bullet-} + {}^{\bullet}OH \rightarrow {}^{1}O_2 + OH^- \tag{25}$$

The consumption of $O_2^{\bullet-}$ radicals is confirmed by an initial decrease in their formation when passing from the bare SnO_2 into the composite catalysts (Figure 9). Further increasing the SnS_2 content leads to a steady growth in superoxide radicals generation.

Thus, it can be concluded that by controlling the composition of SnO_2/SnS_2 photocatalysts, one can adjust the type of ROS generated under illumination to drive the catalyst reactivity toward specific reactions. The scavenger tests revealed clearly that the superoxide radicals play a crucial role in IC photodegradation. However, the prevalence of other ROS ($^{\bullet}OH$ and $^{1}O_2$) in the case of the SnO_2, RS_1:2, and RS_1:1 catalysts may interfere with their reactivity with this dye.

3.5.2. Mechanism of ROS Formation. To rationalize how particular ROS can be generated in the investigated photocatalytic materials, we calculated the energy levels of the valence and conduction band edges (E_{VB} and E_{CB}, respectively) using the following equations:[37]

$$E_{CB} = -\chi_{(SnX_2)} + 0.5E_g - 2.303RT/F \times (IEP - pH) \tag{26}$$

$$E_{VB} = E_{CB} - E_g \tag{27}$$

where SnX_2 represents SnO_2 or SnS_2, E_g is the bandgap value, R is the universal gas constant, T is the absolute temperature, F is the Faraday constant, IEP is the isoelectric point value, and $\chi_{(SnX2)}$ is the Mulliken electronegativity of SnX_2, calculated according to the formula:

$$\chi_{(SnX_2)} = (\chi_{(Sn)}\chi_{(X)}^2)^{1/(1+2)} \tag{28}$$

The bandgap and IEP values used in the calculations were determined experimentally in our previous works[35,36] and are consolidated in Table 3. Since the investigated photocatalyst-IC systems are characterized by different pH values (see Table 3), we assumed pH = 7 for comparison purposes. The results are summarized in Figure 10a and Table S2 (Supporting Information). The calculated E_{VB} and E_{CB} values for experimental conditions (i.e., pH around 4 for SnS_2-based samples and pH = 8.7 for RS) are also presented in Table S2. In the case of IC, the energies of the highest occupied and lowest unoccupied molecular orbitals (HOMO and LUMO, respectively) were determined by CV measurements with ferrocene as an internal standard. A detailed description of this method, along with the obtained results, is provided in the Supporting Information (Text S5, Figures S12−S14, and Table S3). In Figure 10a, the experimentally determined HOMO/LUMO levels of IC are marked as $IC_{(exp.)}$. The theoretically calculated values (marked as $IC_{(theor.)}$)[72] are also included for comparison purposes.

To determine the mechanism of ROS generation, the first thing to consider is the pH of the dye-photocatalyst systems. For RS, the pH of the reaction mixture is basic (8.7), while the surface functionalization of SnO_2 with SnS_2 results in a pH change to acidic (pH ∼ 4). Thus, according to the reaction 12, the superoxide radical predominantly exists in the $O_2^{\bullet-}$ form in the SnO_2−IC system, while for SnS_2-based materials, its protonated $HO_2^{\bullet}$ form prevails. This may also affect the materials' reactivity with indigo carmine. Based on the CB edges calculations, both SnO_2 and SnS_2 nanostructures can generate these ROS via the reaction of oxygen with photogenerated electrons. In the case of RS, this process is presented by eq 1, while for SnS_2-based systems, it occurs according to the reaction 2 (see Table 1).

Regarding $^{\bullet}OH$ radicals, only the VB edge level of SnO_2 enables their formation via the direct reaction of OH^- (or H_2O) with photogenerated holes ("Pathway I" in Figure 10b). The redox potentials of $O_2^{\bullet-}$,H^+/H_2O_2 and H_2O_2,$H^+/^{\bullet}OH$ (E = 0.91 and 0.39 V vs NHE, respectively) reactions suggest that hydroxyl radicals can also be generated via the reduction of $O_2^{\bullet-}$ ("Pathway II"). In the case of bare SnS_2 (SH), in turn, $^{\bullet}OH$ species can be formed solely via the second pathway ($HO_2^{\bullet} \rightarrow H_2O_2 \rightarrow {}^{\bullet}OH$)[11] due to its VB edge level. Other

https://doi.org/10.1021/acs.jpcc.3c08165
J. Phys. Chem. C 2024, 128, 5011−5029

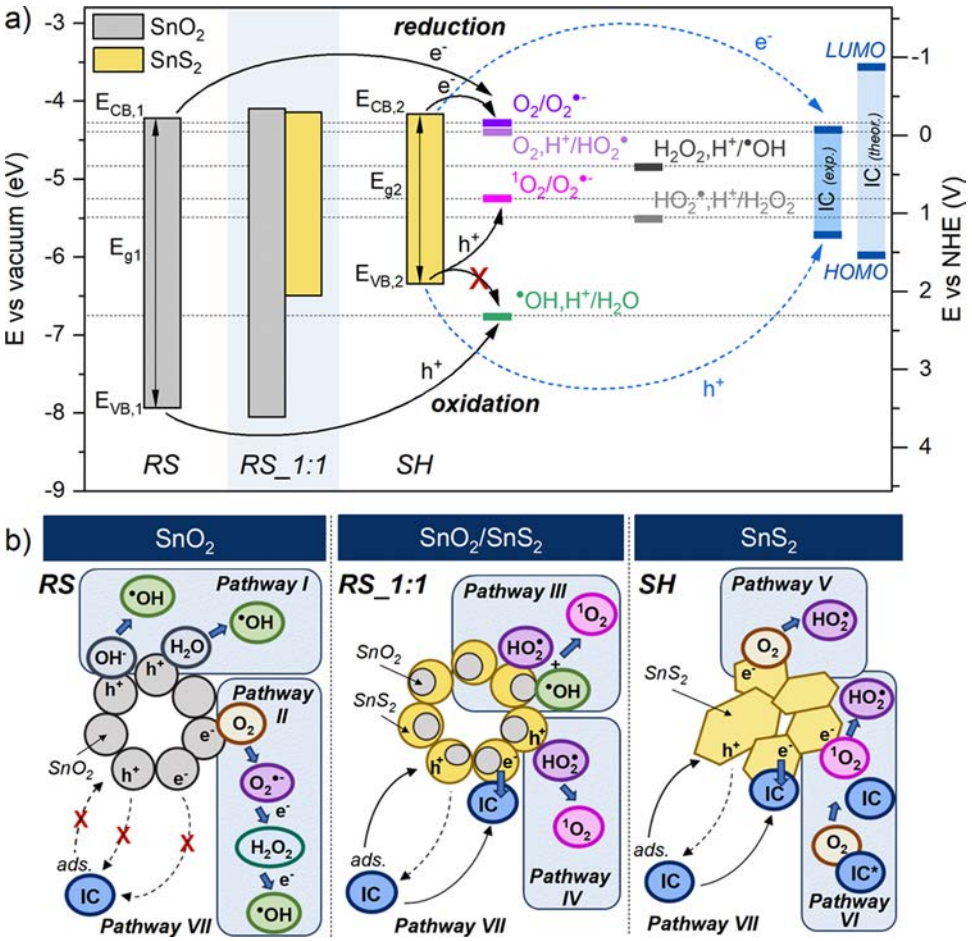

Figure 10. (a) Calculated valence (E_{VB}) and conduction (E_{CB}) band edge levels of SnO_2, SnO_2/SnS_2, and SnS_2 materials (pH = 7) and (b) schematic representation of the predominant ROS generation processes for the selected structures along with their interaction with the IC molecules. The presented ROS formation redox potentials correspond to pH = 7 (except for the reaction O_2,$H^+/HO_2^\bullet$, predominant at pH < 4.8, where the standard redox potential is shown).[10,11,73] The experimentally determined energies of the dye HOMO and LUMO levels are marked as $IC_{(exp.)}$, while the theoretically calculated ones[72] are as $IC_{(theor.)}$.

possible processes of H_2O_2 generation are included in Text S4 (Reactions S3−S5).[10,12] However, the predominant reaction in the SnS_2 sample is described by the "Pathway V" in Figure 10b, in which $HO_2^\bullet$ radicals are generated. This mechanism also prevails for the highest-sulfide-containing SnO_2/SnS_2 composite (RS_2:1).

In the case of the SnO_2/SnS_2 samples characterized by the predominant $^1O_2$ formation, the possible pathways of its generation include (1) the recombination of $HO_2^\bullet$ and $^\bullet OH$ radicals generated over the SnS_2 and SnO_2 photocatalysts, respectively ("Pathway III"); (2) direct oxidation of $HO_2^\bullet$ radicals ("Pathway IV"); and (3) disproportionation of $O_2^{\bullet-}$ and $HO_2^\bullet$ radicals (Text S4, Reaction S2). The obtained results (Figure 9) suggest that "Pathway III" predominates in $^1O_2$ generation because it is most related to the phase composition of the SnO_2/SnS_2 materials. For the bare SnO_2 sample, $^\bullet OH$ radicals are formed preferentially ("Pathway I"). Increasing the SnS_2 content, in turn, leads to more $HO_2^\bullet$ species produced ("Pathway V"). Therefore, it is plausible that for the RS_1:1 sample, $^\bullet OH$ and $HO_2^\bullet$ radicals are generated in comparable amounts, resulting in a preferential $^1O_2$ formation (the combination of "Pathway I" and "Pathway V" leads the predominant "Pathway III").

The redox potential of the $^1O_2/O_2^{\bullet-}$ couple also suggests that $HO_2^\bullet$ oxidation to singlet oxygen ("Pathway IV") and $^1O_2$ reduction to superoxide radicals ("Pathway VI") can compete with each other. This can also affect the change in the mechanism pathway from ($^1O_2$ to $HO_2^\bullet$) between the RS_1:1 and RS_2:1 photocatalysts, as in the case of the latter, more photoelectrons can be generated with an increased fraction of visible-light-active SnS_2 component.

The last aspect to consider is the interaction between the investigated photocatalysts and the IC. The experimentally determined dye LUMO level ($IC_{(exp.)}$, see Figures 10a and S14b, and Table S3) indicates that the photogenerated electrons in the CB of both the SnO_2 and SnS_2 components can participate in the direct reduction of IC ("Pathway VII"). This is consistent with the scavenger tests (Figure 5b) and reveals that electrons do not participate only indirectly in IC degradation (by generating $HO_2^\bullet$ radicals). The theoretical LUMO value ($IC_{(theor.)}$),[72] in turn, could suggest the occurrence of the sensitization-mediated degradation process (injection of e^- from the excited dye molecules, IC*, to the CB of photocatalysts). However, the value of the HOMO−LUMO gap determined from UV−vis spectroscopy (E_{opt} = 1.52 eV, Text S5, Figure S14c), narrower than that from theoretical calculations, is consistent with the CV results (Figure S14b). Therefore, the electron (e^-) transfer direction is marked from the photocatalysts to the dye. In the case of the RS photocatalyst, "Pathway VII" was excluded as the IC molecules

https://doi.org/10.1021/acs.jpcc.3c08165
J. Phys. Chem. C 2024, 128, 5011−5029

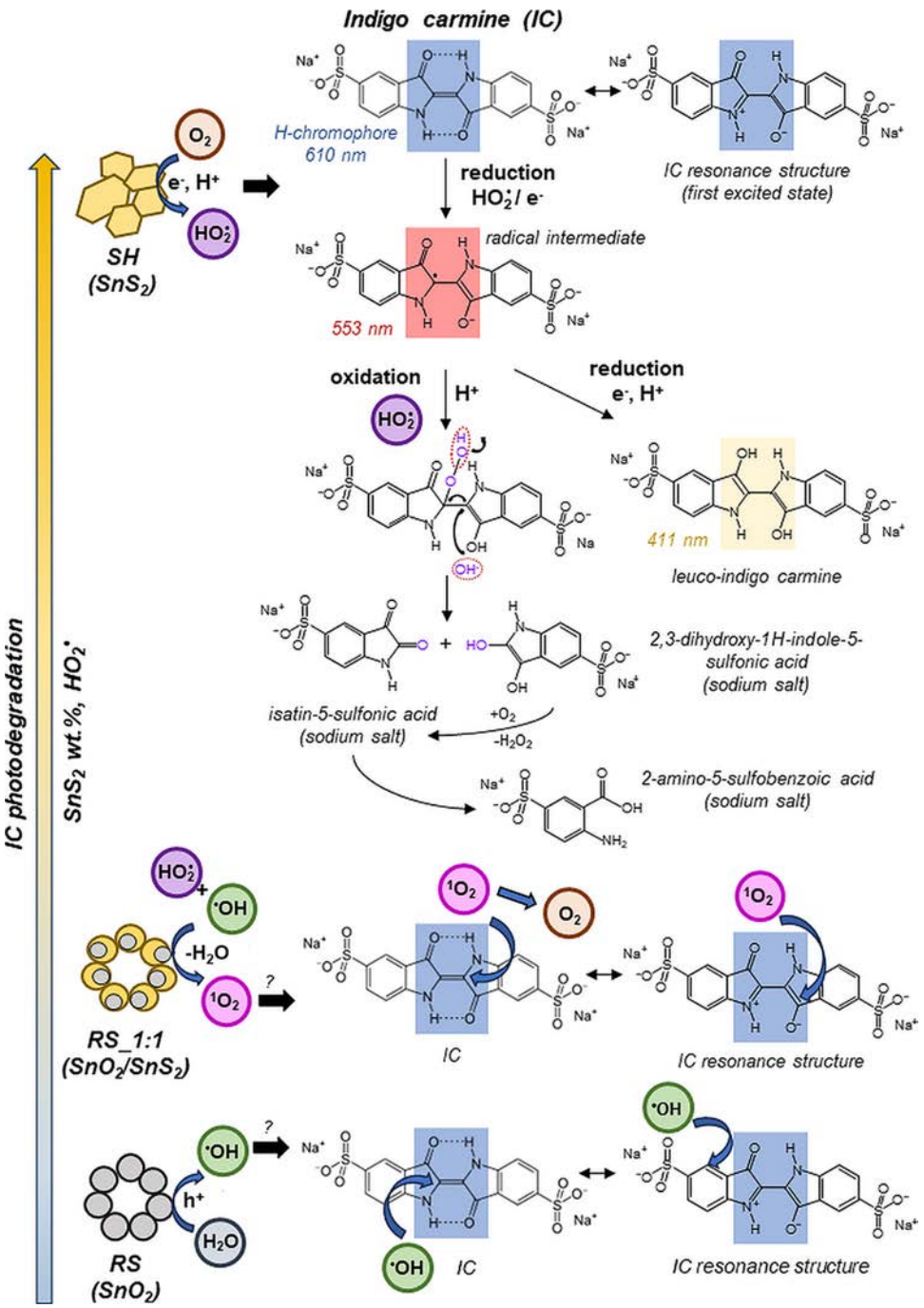

Figure 11. Schematic representation of IC photodegradation mechanism depending on the type of the photocatalytic materials (SnO_2, SnO_2/SnS_2, or SnS_2).

are not readily adsorbed on its surface. The IC HOMO level, in turn, suggests that it can also be degraded via the photogenerated holes. However, the scavenger tests indicated this pathway as insignificant (dashed lines in Figure 10b). Regarding other possible dye interactions in photocatalytic systems, the excited under illumination IC* can transfer energy to oxygen molecules, leading to $^1O_2$ generation (physical quenching), as illustrated by "Pathway VI" in Figure 10b. The formed species can, for example, undergo reduction to $HO_2^\bullet$ radicals.

Taking into account all discussed reactions and obtained results, it can be concluded that (1) once the SnO_2 content in the samples increases, more hydroxyl radicals ($^\bullet OH$) can be produced via the direct oxidation of water by photogenerated holes; (2) when the content of visible-light-active SnS_2 increases, in turn, more $HO_2^\bullet$ radicals can be generated via direct reduction of oxygen by photogenerated electrons; and (3) in the case of SnO_2/SnS_2 heterostructures, the competing processes of $^\bullet OH$ and $HO_2^\bullet$ formation may lead to their recombination, and thus, to singlet oxygen ($^1O_2$) formation. Consequently, in the case of RS (SnO_2), the predominant ROS are $^\bullet OH$ radicals, for RS_1:2 and RS_1:1—singlet oxygen species—and for RS_2:1 and SH (SnS_2)—$HO_2^\bullet$ radicals (see Figure 9). Moreover, the photogenerated electrons over the photocatalysts can participate in direct IC reduction.

https://doi.org/10.1021/acs.jpcc.3c08165
J. Phys. Chem. C 2024, 128, 5011−5029

3.5.3. Postulated Mechanism of IC Degradation. Knowing that the efficiency of IC degradation increases with increasing SnS_2 content (Figure 2) and how ROS speciation and generation efficiency change across all the samples with their changing composition, the IC photodegradation pathways can be proposed (Figure 11) in line with the representative literature.[74−82] Indigo carmine is classified as a donor−acceptor dye type, where heterocyclic amines (−NH− groups) are electron donors, and carbonyl groups (−C═O) are electron acceptors. The color of IC in aqueous solutions (absorbance maximum at 610 nm[77,78]) is related to the structural unit consisting of two −NH− and −C═O groups that are "cross-conjugated" through >C═C< bridge (H-chromophore).[77,83] Under light illumination, dye molecules can be converted into a higher-energy excited state (IC*). One of the five possible resonance structures is shown in Figure 11. In each resonance structure, the negative charge is located on oxygen, while the positive one is on quaternary nitrogen.[77]

The performed experiments revealed that superoxide/hydroperoxyl radicals ($O_2^{\bullet-}/HO_2^{\bullet}$, depending on the solution pH) contribute principally to the IC photodegradation process. This is consistent with recent studies[75,84−86] using CdS, FeS_2, CuS, NiS_2, TiO_2, and TiO_2@g-C_3N_4 photocatalysts, where the minor role of hydroxyl radicals ($^{\bullet}OH$) in the IC degradation has also been asserted. However, for TiO_2-based catalysts,[85,86] a significant contribution of photogenerated holes (h^+) to this process has been reported. In the case of our materials, such an effect was not observed, as evidenced by the scavenger tests. Instead, the quenching experiments suggested the participation of photogenerated electrons (e^-) in the IC degradation reaction, which is consistent with the determined E_{CB} and LUMO energy levels of the photocatalysts and IC, respectively. In addition to $O_2^{\bullet-}/HO_2^{\bullet}$ radicals, which degrade efficiently the dye molecules, these species (e^-) can convert IC to pale yellow leuco-IC (absorbance maximum at 411 nm) via two-step reduction (Figure 11). The intermediate product is a red-colored radical (absorbance maximum at 553 nm). However, it is difficult to detect the corresponding color change during the reduction process.[87] In the case of SH (SnS_2), the observed slight increase in absorption at ca. 410 nm may suggest the presence of leuco-IC (see Figure S15 in the Supporting Information).

Nevertheless, the process mainly responsible for IC degradation involves the reaction of the dye molecules with superoxide/hydroperoxyl radicals ($O_2^{\bullet-}/HO_2^{\bullet}$), whose mechanism has been established in the literature.[74,75] The possible pathway of the IC reaction with $HO_2^{\bullet}$· radicals (generated in SnS_2-based systems) is presented in Figure 11. This radical can act both as an oxidizing and one-electron-reducing agent.[12] The first step of IC degradation involves its one-electron reduction to the previously described radical intermediate. It is oxidized subsequently into isatin-5-sulfonic acid and 2,3-dihydroxy-1H-indole-5-sulfonic acid (or their sodium salts). The latter compound is auto-oxidized into the former. When substantial amounts of $HO_2^{\bullet}$ radicals are formed, isatin-5-sulfonic acid can be further oxidized into 2-amino-5-sulfobenzoic acid and then be mineralized even completely.[75]

As the SnS_2 content decreases in the samples (dropping the amount of generated $HO_2^{\bullet}$ radicals), the IC degradation/decolorization is less effective. For RS (SnO_2) and RS_1:1 (SnO_2/SnS_2), the predominant ROS are hydroxyl radicals ($^{\bullet}OH$) and singlet oxygen molecules, respectively. These species ($^{\bullet}OH$, $^1O_2$) may also participate in the IC photodegradation process. However, little about the possible mechanisms of such reaction pathways is known. Redox potential values (Table 1) suggest that, among ROS, hydroxyl radical ($^{\bullet}OH$) is the most powerful oxidizing agent. Therefore, it is often considered the most effective species for photodegradation processes.[10] Noteworthy, the $^{\bullet}OH$ radical is nonselective, which means it can oxidize virtually any molecule. Therefore, its reactivity does not always result in a high photodegradation efficiency, as many competing reactions can proceed simultaneously in such systems.[88] Consequently, in the case of RS, the IC degradation process was characterized by the lowest efficiency (Figures 2 and S3). Other factors that inhibited the dye decomposition were the adsorptive properties of this sample toward IC and its bandgap value (Figure 10b). Regarding possible interactions of generated $^{\bullet}OH$ radicals with the IC molecules, so far, a comprehensive mechanism has not been proposed. Zhou et al. analyzed the indigo photodegradation process (analogous molecule to IC, but without $-SO_3^-$ groups). Based on DFT calculations, it was suggested that these radicals most probably can attack both >C═C< bond and C atoms in benzene rings.[79]

In the case of singlet oxygen interactions with various substances, this ROS can transfer energy to them without forming new products (physical quenching to the ground state $^3O_2$) or undergo a chemical reaction, such as cycloaddition (chemical quenching).[89] Therefore, it can simply transfer energy to IC molecules without dye decolorization (the opposite reaction, IC* + $^3O_2$ → IC + $^1O_2$, is also possible—see Figure 10b, "Pathway VI"). Regarding its chemical quenching process, Zhang et al.[80] suggested the mechanism of $^1O_2$ addition to indoles (via double bond in a five-membered ring containing nitrogen, R−C═C−R). Kuramoto and Kitao[81] proposed the possible indigo photodegradation pathway via the addition of $^1O_2$ molecule to >C═C< bond, leading to the formation of isatin. The possible C atoms that may preferably be attacked by $^{\bullet}OH$ and $^1O_2$ are schematically marked in Figure 11.

Based on the proposed mechanisms, it seems that $^{\bullet}OH$ and $^1O_2$ may also contribute to the IC degradation (or decolorization) process. However, the results of this study suggest that in the case of SnO_2/SnS_2-based catalysts, these processes are less effective than $HO_2^{\bullet}$-mediated photodegradation. Thus, the nature of predominant radicals generated in a controlled manner by varying the SnO_2/SnS_2 composition is crucial in adjusting the reactivity of the designed photocatalysts in photodegradation reactions of various contaminants.

4. CONCLUSIONS

In summary, the obtained results revealed the possibility of tunable ROS generation in the SnO_2/SnS_2-based nanomaterials. By modifying the phase composition of the samples from pure SnO_2 through SnO_2/SnS_2 composites to SnS_2, their activity in the formation of reactive species changes as follows: from $^{\bullet}OH$ (RS) through $^1O_2$ (RS_1:2, RS_1:1) to $O_2^{\bullet-}/HO_2^{\bullet}$ (RS_2:1, SH). The $^{\bullet}OH$ radicals are generated mainly via the oxidation of OH^-/H_2O with the photogenerated h^+ in the VB of SnO_2, while the $O_2^{\bullet-}$ ($HO_2^{\bullet}$) species are formed predominantly via the one-electron reduction of molecular oxygen (photoelectrons generated in the CB of SnS_2). In the case of SnO_2/SnS_2 heterostructures, the simultaneous formation of $O_2^{\bullet-}$ ($HO_2^{\bullet}$) and $^{\bullet}OH$ radicals leads to their

https://doi.org/10.1021/acs.jpcc.3c08165
J. Phys. Chem. C 2024, 128, 5011−5029

recombination and, consequently, singlet oxygen generation. When the fraction of visible-light-active SnS_2 component increases, more photoelectrons and superoxide radicals are generated, which results in a change in the mechanism pathway. The scavenger tests indicated that IC dye is degraded predominantly by $O_2^{\bullet-}$ ($HO_2^{\bullet}$) species and, to some extent, photogenerated electrons. The prevalence of other ROS ($^{\bullet}OH$ and $^1O_2$) in the RS, RS_1:2, and RS_1:1 samples interfere with the reactivity of superoxide radicals with IC, inhibiting its photodecomposition. Moreover, quenching experiments revealed that various side processes occur in photocatalytic systems with scavengers, which should always be considered when analyzing the results.

The conducted scavenger tests showed that these substances can (1) react with dyes under illumination as a result of their photolysis (e.g., $AgNO_3$, $K_2S_2O_8$, pBQ); (2) generate additional radicals that degrade dyes (e.g., NaN_3 by scavenging $^1O_2$ can produce $O_2^{\bullet-}$, and TBA/MeOH via reacting with $^{\bullet}OH$ − hydroxyalkyl radicals, resulting in the promotion of IC photodegradation process); (3) affect dye adsorption on the photocatalyst's surface by electrostatic forces and, consequently, change the photodegradation efficiency (e.g., electrostatic repulsion between $Cr_2O_7^{2-}$ and anionic IC caused increased dye adsorption on the SH surface and promoted IC photodegradation); (4) be degraded by other ROS (e.g., $K_2Cr_2O_7$ by $O_2^{\bullet-}$); (5) react with photocatalysts, changing their surface properties ($AgNO_3$ can react with SnS_2 to form Ag_2S via in situ ion exchange, resulting in immediate precipitation of a black powder). Consequently, side reactions can overlap the quenching effect. Therefore, it is crucial to individually adjust scavenger concentrations for each photocatalyst and observe trends (i.e., how changing the scavenger concentration affects the observed quenching effect).

EPR spin trapping measurements with DMPO showed that the higher the SnO_2 fraction in the samples, the more $^{\bullet}OH$ radicals are generated. Furthermore, these tests gave insight into another possible pathway of this species formation (through the reduction of $O_2^{\bullet-}$ radicals), consistent with quenching experiments. However, if the EPR tests were performed alone, they could lead to misleading conclusions about $O_2^{\bullet-}$ radical generation. Assessment of the $^1O_2$ generation was carried out with TEMP oxidation, which showed a change in the ROS formation mechanism pathway to superoxide radicals for the high-sulfide-containing materials. The adapted NBT assay complemented the EPR and scavenger tests. It confirmed the highest activity of SnS_2 toward superoxide radical generation, as well as the competition between $^1O_2$ and $O_2^{\bullet-}$ formation.

The conducted experiments have demonstrated the importance of using multiple techniques to examine the formation of reactive oxygen species. Variations in ROS generation can lead to different photodegradation mechanisms and affect the process efficiency. Therefore, studying a material's activity toward specific ROS formation and ROS−contaminant interactions could aid in designing photocatalysts with high selectivity in the future.

■ ASSOCIATED CONTENT

Supporting Information

The Supporting Information is available free of charge at https://pubs.acs.org/doi/10.1021/acs.jpcc.3c08165.

Experimental data (Texts S1−S3−chemicals, materials characterization techniques, determination of the dye HOMO and LUMO levels) and the results related to scavenger tests (dye-scavenger interactions, adjustment of scavenger concentrations for the samples, photocatalytic tests with the SnO_2 sample under UV−vis and UV illumination, experiments with quenching agents excluded from further analysis, XRD analysis of the SnS_2 sample before and after photocatalytic tests with $Cu(NO_3)_2$, Figures S1−S5), EPR measurements (EPR spectra and kinetic EPR spectra using DMPO and TEMP as spin traps, Figures S6−S10, Table S1), NBT assay (UV−vis spectra, Figure S11), UV−vis spectra of IC photodegradation (Figure S15), calculated valence and conduction band edge potentials (E_{VB} and E_{CB}, respectively − Table S2) of the analyzed samples, and CV (and optical) measurements for HOMO/LUMO energy levels determination of indigo carmine (Text S5, Figures S12−S14, Table S3). The additional reactions with ROS are also included − Text S4 (PDF)

■ AUTHOR INFORMATION

Corresponding Authors

Kinga Michalec − *Faculty of Materials Science and Ceramics, AGH University of Krakow, Krakow 30-059, Poland;* orcid.org/0000-0002-1654-1800; Email: kmichalec@agh.edu.pl

Bartosz Mozgawa − *Faculty of Chemistry, Jagiellonian University, Krakow 30-387, Poland; Doctoral School of Exact and Natural Sciences, Jagiellonian University, Krakow 30-348, Poland;* orcid.org/0000-0002-7818-7210; Email: bartosz.mozgawa@doctoral.uj.edu.pl

Authors

Anna Kusior − *Faculty of Materials Science and Ceramics, AGH University of Krakow, Krakow 30-059, Poland;* orcid.org/0000-0002-1730-7610

Piotr Pietrzyk − *Faculty of Chemistry, Jagiellonian University, Krakow 30-387, Poland;* orcid.org/0000-0002-7808-1280

Zbigniew Sojka − *Faculty of Chemistry, Jagiellonian University, Krakow 30-387, Poland;* orcid.org/0000-0001-7226-7626

Marta Radecka − *Faculty of Materials Science and Ceramics, AGH University of Krakow, Krakow 30-059, Poland*

Complete contact information is available at: https://pubs.acs.org/10.1021/acs.jpcc.3c08165

Notes

The authors declare no competing financial interest.

■ ACKNOWLEDGMENTS

This work was supported by The Ministry of Education and Science in Poland, grant number DI2018 008148 (K.M.) and program "Excellence initiative−research university" for the University of Science and Technology (M.R. and A.K.).

■ REFERENCES

(1) Priyadarshini, M.; Das, I.; Ghangrekar, M. M.; Blaney, L. Advanced Oxidation Processes: Performance, Advantages, and Scale-up of Emerging Technologies. *J. Environ. Manage.* **2022**, *316*, 115295.
(2) Liu, L.; Chen, Z.; Zhang, J.; Shan, D.; Wu, Y.; Bai, L.; Wang, B. Treatment of Industrial Dye Wastewater and Pharmaceutical Residue

Wastewater by Advanced Oxidation Processes and Its Combination with Nanocatalysts: A Review. *J. Water Process Eng.* **2021**, *42* (22), 102122.
(3) Ma, D.; Yi, H.; Lai, C.; Liu, X.; Huo, X.; An, Z.; Li, L.; Fu, Y.; Li, B.; Zhang, M.; et al. Critical Review of Advanced Oxidation Processes in Organic Wastewater Treatment. *Chemosphere* **2021**, *275*, 130104.
(4) Dewil, R.; Mantzavinos, D.; Poulios, I.; Rodrigo, M. A. New Perspectives for Advanced Oxidation Processes. *J. Environ. Manage.* **2017**, *195*, 93−99.
(5) Goodarzi, N.; Ashrafi-peyman, Z.; Khani, E.; Moshfegh, A. Z. Recent Progress on Semiconductor Heterogeneous Photocatalysts in Clean Energy Production and Environmental Remediation. *Catalysts* **2023**, *13* (7), 1102.
(6) Friedmann, D. A General Overview of Heterogeneous Photocatalysis as a Remediation Technology for Wastewaters Containing Pharmaceutical Compounds. *Water* **2022**, *14* (21), 3588.
(7) Dong, C.; Fang, W.; Yi, Q.; Zhang, J. A Comprehensive Review on Reactive Oxygen Species (ROS) in Advanced Oxidation Processes (AOPs). *Chemosphere* **2022**, *308*, 136205.
(8) Wang, J.; Wang, S. Reactive Species in Advanced Oxidation Processes: Formation, Identification and Reaction Mechanism. *Chem. Eng. J.* **2020**, *401*, 126158.
(9) He, W.; Jia, H.; Wamer, W. G.; Zheng, Z.; Li, P.; Callahan, J. H.; Yin, J. J. Predicting and Identifying Reactive Oxygen Species and Electrons for Photocatalytic Metal Sulfide Micro-Nano Structures. *J. Catal.* **2014**, *320*, 97−105.
(10) Nosaka, Y.; Nosaka, A. Y. Generation and Detection of Reactive Oxygen Species in Photocatalysis. *Chem. Rev.* **2017**, *117* (17), 11302−11336.
(11) Koppenol, W. H.; Stanbury, D. M.; Bounds, P. L. Electrode Potentials of Partially Reduced Oxygen Species, from Dioxygen to Water. *Free Radic. Biol. Med.* **2010**, *49* (3), 317−322.
(12) Hayyan, M.; Hashim, M. A.; Alnashef, I. M. Superoxide Ion: Generation and Chemical Implications. *Chem. Rev.* **2016**, *116* (5), 3029−3085.
(13) Martemucci, G.; Costagliola, C.; Mariano, M.; D'andrea, L.; Napolitano, P.; D'alessandro, A. G. Free Radical Properties, Source and Targets Antioxidant Consumption and Health. *Oxygen* **2022**, *2* (2), 48−78.
(14) Andrés, C. M. C.; Pérez de la lastra, J. M.; Andrés juan, C.; Plou, F. J.; Pérez-lebeña, E. Superoxide Anion Chemistry—Its Role at the Core of the Innate Immunity. *Int. J. Mol. Sci.* **2023**, *24* (3), 1841.
(15) Durand, G.; Choteau, F.; Pucci, B.; Villamena, F. A. Reactivity of Superoxide Radical Anion and Hydroperoxyl Radical with α-Phenyl-N-Tert-Butylnitrone (PBN) Derivatives. *J. Phys. Chem. A* **2008**, *112* (48), 12498−12509.
(16) Wang, L.; Lan, X.; Peng, W.; Wang, Z. Uncertainty and Misinterpretation over Identification, Quantification and Transformation of Reactive Species Generated in Catalytic Oxidation Processes: A Review. *J. Hazard. Mater.* **2021**, *408*, 124436.
(17) Liu, W.; Lu, Y.; Dong, Y.; Jin, Q.; Lin, H. A Critical Review on Reliability of Quenching Experiment in Advanced Oxidation Processes. *Chem. Eng. J.* **2023**, *466*, 143161.
(18) Schneider, J. T.; Firak, D. S.; Ribeiro, R. R.; Peralta-zamora, P. Use of Scavenger Agents in Heterogeneous Photocatalysis: Truths, Half-Truths, and Misinterpretations. *Phys. Chem. Chem. Phys.* **2020**, *22* (27), 15723−15733.
(19) Gao, Z.; Zhang, D.; Jun, Y. S. Does Tert-Butyl Alcohol Really Terminate the Oxidative Activity of ·OH in Inorganic Redox Chemistry? *Environ. Sci. Technol.* **2021**, *55* (15), 10442−10450.
(20) Babu, B.; Neelakanta reddy, I.; Yoo, K.; Kim, D.; Shim, J. Bandgap Tuning and XPS Study of SnO_2 Quantum Dots. *Mater. Lett.* **2018**, *221*, 211−215.
(21) Park, J.; Saidi, W. A.; Chorpening, B.; Duan, Y. Quantifying Temperature Dependence of Electronic Band Gaps and Optical Properties in SnO_2 and SnO via First-Principles Simulations. *J. Phys. Chem. C* **2021**, *125* (40), 22231−22238.
(22) Zhou, W.; Liu, Y.; Yang, Y.; Wu, P. Band Gap Engineering of SnO_2 by Epitaxial Strain: Experimental and Theoretical Investigations. *J. Phys. Chem. C* **2014**, *118* (12), 6448−6453.
(23) Whittles, T. J.; Burton, L. A.; Skelton, J. M.; Walsh, A.; Veal, T. D.; Dhanak, V. R. Band Alignments, Valence Bands, and Core Levels in the Tin Sulfides SnS, SnS_2, and Sn_2S_3: Experiment and Theory. *Chem. Mater.* **2016**, *28* (11), 3718−3726.
(24) Zhao, W.; He, M.; Chen, F.; Jin, X.; Duan, H.; Long, M.; Wu, Z.; Cao, B.; Yu, Y. One-Pot Synthesis of Flower-like SnS_2/SnO_2 Heterojunction with Enhanced Visible Light Photocatalytic Performance. *Opt. Mater. (Amst).* **2022**, *123*, 111934.
(25) Sharma, K.; Patial, S.; Singh, P.; Khan, A. A. P.; Saini, V.; Nadda, A. K.; Hussain, C. M.; Nguyen, V. H.; Nguyen, C. C.; Hac nguyen, T. B.; et al. Strategies and Perspectives of Tailored SnS_2 Photocatalyst for Solar Driven Energy Applications. *Sol. Energy* **2022**, *231*, 546−565.
(26) Cheng, Y.; Tang, P.; Liang, P.; Liu, X.; Cao, D.; Chen, X.; Shu, H. Sulfur-Driven Transition from Vertical to Lateral Growth of 2D SnS−SnS_2 Heterostructures and Their Band Alignments. *J. Phys. Chem. C* **2020**, *124* (50), 27820−27828.
(27) Sun, C.; Yang, J.; Xu, M.; Cui, Y.; Ren, W.; Zhang, J.; Zhao, H.; Liang, B. Recent Intensification Strategies of SnO_2-Based Photocatalysts: A Review. *Chem. Eng. J.* **2022**, *427*, 131564.
(28) Sunaina; Yadav, K. K.; Ankush; Guchhait, S. K.; Sood, K.; Mehta, S. K.; Ganguli, A. K.; Jha, M. Mechanistic Insights of Enhanced Photocatalytic Efficiency of SnO_2-SnS_2 Heterostructures Derived from Partial Sulphurization of SnO_2. *Sep. Purif. Technol.* **2020**, *242*, 116835.
(29) Ren, W.; Yang, J.; Chen, W.; Zhang, J.; Sun, Y.; Zheng, Y.; Zhao, H.; Liang, B. In Situ Synthesis of Novel 0D/ 2D SnO_2 Nanoparticles/ SnS_2 Nanosheets S-Scheme Heterojunction for Enhancing the Photocatalytic Pollutant Degradation. *Mater. Res. Bull.* **2022**, *153*, 111884.
(30) Guo, Z.; Ambrosio, F.; Chen, W.; Gono, P.; Pasquarello, A. Alignment of Redox Levels at Semiconductor-Water Interfaces. *Chem. Mater.* **2018**, *30* (1), 94−111.
(31) Pinto, A. H.; Nogueira, A. E.; Dalmaschio, C. J.; Frigini, I. N.; De almeida, J. C.; Ferrer, M. M.; Berengue, O. M.; Gonçalves, R. A.; De mendonça, V. R. Doped Tin Dioxide (d-SnO_2) and Its Nanostructures: Review of the Theoretical Aspects Photocatalytic and Biomedical Applications. *Solids* **2022**, *3* (2), 327−360.
(32) Joe, J.; Yang, H.; Bae, C.; Shin, H. Metal Chalcogenides on Silicon Photocathodes for Efficient Water Splitting: A Mini Overview. *Catalysts* **2019**, *9* (2), 149.
(33) He, W.; Jia, H.; Cai, J.; Han, X.; Zheng, Z.; Wamer, W. G.; Yin, J. J. Production of Reactive Oxygen Species and Electrons from Photoexcited ZnO and ZnS Nanoparticles: A Comparative Study for Unraveling Their Distinct Photocatalytic Activities. *J. Phys. Chem. C* **2016**, *120* (6), 3187−3195.
(34) He, W.; Jia, H.; Yang, D.; Xiao, P.; Fan, X.; Zheng, Z.; Kim, H. K.; Wamer, W. G.; Yin, J. J. Composition Directed Generation of Reactive Oxygen Species in Irradiated Mixed Metal Sulfides Correlated with Their Photocatalytic Activities. *ACS Appl. Mater. Interfaces* **2015**, *7* (30), 16440−16449.
(35) Michalec, K.; Kusior, A.; Mikuła, A.; Radecka, M. New Insights into the Formation of Multi-Core−Shell Mesoporous SnO_2@SnS_2 Nanostructures. *Mater. Res. Lett.* **2021**, *9* (10), 445−451.
(36) Michalec, K.; Kusior, A. From Adsorbent to Photocatalyst: The Sensitization Effect of SnO_2 Surface towards Dye Photodecomposition. *Molecules* **2021**, *26* (23), 7123.
(37) Zhang, L.; Jaroniec, M. Toward Designing Semiconductor-Semiconductor Heterojunctions for Photocatalytic Applications. *Appl. Surf. Sci.* **2018**, *430*, 2−17.
(38) Kissling, G. P.; Ruhstaller, B.; Pernstich, K. P. Measuring Frontier Orbital Energy Levels of OLED Materials Using Cyclic Voltammetry in Solution. *Org. Electron.* **2023**, *122*, 106888.
(39) Thorat, K. G.; Kamble, P.; Ray, A. K.; Sekar, N. Novel Pyrromethene Dyes with N-Ethyl Carbazole at the Meso Position: A

https://doi.org/10.1021/acs.jpcc.3c08165
J. Phys. Chem. C 2024, 128, 5011−5029

Comprehensive Photophysical, Lasing, Photostability and TD-DFT Study. *Phys. Chem. Chem. Phys.* **2015**, *17* (26), 17221−17236.
(40) Spałek, T.; Pietrzyk, P.; Sojka, Z. Application of the Genetic Algorithm Joint with the Powell Method to Nonlinear Least-Squares Fitting of Powder EPR Spectra. *J. Chem. Inf. Model.* **2005**, *45* (1), 18−29.
(41) Ghosh chaudhuri, R.; Paria, S. Core/Shell Nanoparticles: Classes, Properties, Synthesis Mechanisms, Characterization, and Applications. *Chem. Rev.* **2012**, *112* (4), 2373−2433.
(42) Gola, D.; Kriti, A.; Bhatt, N.; Bajpai, M.; Singh, A.; Arya, A.; Chauhan, N.; Srivastava, S. K.; Tyagi, P. K.; Agrawal, Y. Silver Nanoparticles for Enhanced Dye Degradation. *Curr. Res. Green Sustain. Chem.* **2021**, *4*, 100132.
(43) Schneider, J.; Bahnemann, D. W. Undesired Role of Sacrificial Reagents in Photocatalysis. *J. Phys. Chem. Lett.* **2013**, *4* (20), 3479−3483.
(44) Fónagy, O.; Szabó-bárdos, E.; Horváth, O. 1,4-Benzoquinone and 1,4-Hydroquinone Based Determination of Electron and Superoxide Radical Formed in Heterogeneous Photocatalytic Systems. *J. Photochem. Photobiol. A Chem.* **2021**, *407*, 113057.
(45) Zhu, M.; Lu, J.; Hu, Y.; Liu, Y.; Hu, S.; Zhu, C. Photochemical Reactions between 1,4-Benzoquinone and $O_2^{\cdot-}$. *Environ. Sci. Pollut. Res.* **2020**, *27* (25), 31289−31299.
(46) Dou, K.; Peng, C.; Wang, R.; Cao, H.; Yao, C.; Qiu, J.; Liu, J.; Tsidaeva, N.; Wang, W. S-Scheme Tubular g-C_3N_4/BiOI Heterojunctions for Boosting Photodegradation of Tetracycline and Cr(VI): Mechanism Insight, Degradation Pathway and DFT Calculation. *Chem. Eng. J.* **2023**, *455*, 140813.
(47) Liu, Y.; Geng, P.; Wang, J.; Yang, Z.; Lu, H.; Hai, J.; Lu, Z.; Fan, D.; Li, M. In-Situ Ion-Exchange Synthesis Ag_2S Modified SnS_2 Nanosheets toward Highly Photocurrent Response and Photocatalytic Activity. *J. Colloid Interface Sci.* **2018**, *512*, 784−791.
(48) Taniguchi, H.; Madden, K. P. An in Situ Radiolysis Time-Resolved ESR Study of the Kinetics of Spin Trapping by 5,5-Dimethyl-1-Pyrroline-N-Oxide. *J. Am. Chem. Soc.* **1999**, *121* (50), 11875−11879.
(49) Samad, A.; Ahsan, S.; Tateishi, I.; Furukawa, M.; Katsumata, H.; Suzuki, T.; Kaneco, S. Indirect Photocatalytic Reduction of Arsenate to Arsenite in Aqueous Solution with TiO_2 in the Presence of Hole Scavengers. *Chin. J. Chem. Eng.* **2018**, *26* (3), 529−533.
(50) Fontana, F.; Holt, R. J.; Huang, Y.; Wayner, D. D. M. Organic Reducing Agents: Some Radical Chain Reactions of Ketyl and 1,3-Dioxolanyl Radicals with Activated Bromides. *J. Org. Chem.* **1994**, *59* (16), 4671−4676.
(51) Wang, Z.; Ma, W.; Chen, C.; Ji, H.; Zhao, J. Probing Paramagnetic Species in Titania-Based Heterogeneous Photocatalysis by Electron Spin Resonance (ESR) Spectroscopy-A Mini Review. *Chem. Eng. J.* **2011**, *170* (2−3), 353−362.
(52) Chen, L.; Duan, J.; Du, P.; Sun, W.; Lai, B.; Liu, W. Accurate Identification of Radicals by In-Situ Electron Paramagnetic Resonance in Ultraviolet-Based Homogenous Advanced Oxidation Processes. *Water Res.* **2022**, *221*, 118747.
(53) Finkelstein, E.; Rosen, G. M.; Rauckman, E. J. Spin Trapping. Kinetics of the Reaction of Superoxide and Hydroxyl Radicals with Nitrones. *J. Am. Chem. Soc.* **1980**, *102* (15), 4994−4999.
(54) Jurva, U.; Wikström, H. V.; Bruins, A. P. Electrochemically Assisted Fenton Reaction: Reaction of Hydroxyl Radicals with Xenobiotics Followed by on-Line Analysis with High-Performance Liquid Chromatography/Tandem Mass Spectrometry. *Rapid Commun. Mass Spectrom.* **2002**, *16* (20), 1934−1940.
(55) Li, Y.; Lu, J.; Wang, X.; Zhang, H.; Wu, X.; Zhang, K. H. L.; Ye, J.; Zhan, D. Direct Conversion of Methanol to Ethanol on the Metal-Carbon Interface. *ChemCatChem.* **2019**, *11* (9), 2277−2282.
(56) Burkitt, M.; Tsang, S. Y.; Tam, S. C.; Bremner, I. Generation of 5,5-Dimethyl-1-PyrrolineN-Oxide Hydroxyl and Scavenger Radical Adducts from Copper/H_2O_2 Mixtures: Effects of Metal Ion Chelation and the Search for High-Valent Metal−Oxygen Intermediates. *Arch. Biochem. Biophys.* **1995**, *323* (1), 63−70.
(57) Niu, M.; Huang, F.; Cui, L.; Huang, P.; Yu, Y.; Wang, Y. Hydrothermal Synthesis, Structural Characteristics, and Enhanced Photocatalysis of SnO_2/α-Fe_2O_3 Semiconductor Nanoheterostructures. *ACS Nano* **2010**, *4* (2), 681−688.
(58) Sun, M.; Su, Y.; Du, C.; Zhao, Q.; Liu, Z. Self-Doping for Visible Light Photocatalytic Purposes: Construction of SiO_2/SnO_2/SnO_2:Sn^{2+} Nanostructures with Tunable Optical and Photocatalytic Performance. *RSC Adv.* **2014**, *4* (58), 30820−30827.
(59) Sun, Y.; Zhu, Q.; Bai, B.; Li, Y.; He, C. Novel All-Solid-State Z-Scheme SnO_2/Pt/In_2O_3 Photocatalyst with Boosted Photocatalytic Performance on Water Splitting and 2,4-Dichlorophenol Degradation under Visible Light. *Chem. Eng. J.* **2020**, *390*, 124518.
(60) Devi, L. G.; Shyamala, R. Photocatalytic Activity of SnO_2-α-Fe_2O_3 Composite Mixtures: Exploration of Number of Active Sites, Turnover Number and Turnover Frequency. *Mater. Chem. Front.* **2018**, *2* (4), 796−806.
(61) Aslam, M.; Tariq qamar, M.; Ali, S.; Rehman, A. U.; Soomro, M. T.; Ahmed, I.; Ismail, I. M. I.; Hameed, A. Evaluation of SnO_2 for Sunlight Photocatalytic Decontamination of Water. *J. Environ. Manage.* **2018**, *217*, 805−814.
(62) Liu, J.; Zhang, Q.; Tian, X.; Hong, Y.; Nie, Y.; Su, N.; Jin, G.; Zhai, Z.; Fu, C. Highly Efficient Photocatalytic Degradation of Oil Pollutants by Oxygen Deficient SnO_2 Quantum Dots for Water Remediation. *Chem. Eng. J.* **2021**, *404*, 127146.
(63) Bandara, J.; Ranasinghe, R. A. S. S. The Effect of MgO Coating on Photocatalytic Activity of SnO_2 for the Degradation of Chlorophenol and Textile Colorants; the Correlation between the Photocatalytic Activity and the Negative Shift of Flatband Potential of SnO_2. *Appl. Catal. A Gen.* **2007**, *319*, 58−63.
(64) Ilan, Y. A.; Czapski, G.; Meisel, D. The One-Electron Transfer Redox Potentials of Free Radicals. I. The Oxygen/Superoxide System. *Biochim. Biophys. Acta (BBA)-Bioenergetics* **1976**, *430* (2), 209−224.
(65) Scurlock, R. D.; Wang, B.; Ogilby, P. R.; Sheats, J. R.; Clough, R. L. Singlet Oxygen as a Reactive Intermediate in the Photodegradation of an Electroluminescent Polymer. *J. Am. Chem. Soc.* **1995**, *117* (41), 10194−10202.
(66) Wang, C.; Zhang, M.; Fang, Y.; Chen, G.; Li, Q.; Sheng, X.; Xu, X.; Hui, J.; Lan, Y.; Fang, M.; et al. SbSI Nanocrystals: An Excellent Visible Light Photocatalyst with Efficient Generation of Singlet Oxygen. *ACS Sustain. Chem. Eng.* **2018**, *6* (9), 12166−12175.
(67) Nardi, G.; Manet, I.; Monti, S.; Miranda, M. A.; Lhiaubet-vallet, V. Scope and Limitations of the TEMPO/EPR Method for Singlet Oxygen Detection: The Misleading Role of Electron Transfer. *Free Radic. Biol. Med.* **2014**, *77*, 64−70.
(68) Samuni, A.; Krishna, C. M.; Mitchell, J. B.; Collins, C. R.; Russo, A. Superoxide Reaction with Nitroxides. *Free Radic. Res.* **1990**, *9* (3−6), 241−249.
(69) Villamena, F. A.; Das, A.; Nash, K. M. Potential Implication of the Chemical Properties and Bioactivity of Nitrone Spin Traps for Therapeutics. *Future Med. Chem.* **2012**, *4* (9), 1171−1207.
(70) Laight, D. W.; Andrews, T. J.; Haj-yehia, A. I.; Carrier, M. J.; Änggård, E. E. Microassay of Superoxide Anion Scavenging Activity in Vitro. *Environ. Toxicol. Pharmacol.* **1997**, *3* (1), 65−68.
(71) Berridge, M. V.; Herst, P. M.; Tan, A. S. Tetrazolium Dyes as Tools in Cell Biology: New Insights into Their Cellular Reduction. *Biotechnol. Annu. Rev.* **2005**, *11*, 127−152.
(72) El-mansy, M. A. M. Quantum Chemical Studies on Structural, Vibrational, Nonlinear Optical Properties and Chemical Reactivity of Indigo Carmine Dye. *Spectrochim. Acta, Part A Mol. Biomol. Spectrosc.* **2017**, *183*, 284−290.
(73) Wang, L.; Xiao, K.; Zhao, H. The Debatable Role of Singlet Oxygen in Persulfate-Based Advanced Oxidation Processes. *Water Res.* **2023**, *235*, 119925.
(74) Kettle, A. J.; Clark, B. M.; Winterbourn, C. C. Superoxide Converts Indigo Carmine to Isatin Sulfonic Acid: Implications for the Hypothesis That Neutrophils Produce Ozone. *J. Biol. Chem.* **2004**, *279* (18), 18521−18525.
(75) Hernández-gordillo, A.; Rodríguez-gonzález, V.; Oros-ruiz, S.; Gómez, R. Photodegradation of Indigo Carmine Dye by CdS

https://doi.org/10.1021/acs.jpcc.3c08165
J. Phys. Chem. C 2024, 128, 5011−5029

Nanostructures under Blue-Light Irradiation Emitted by LEDs. *Catal. Today* **2016**, *266*, 27−35.
(76) Tello-burgos, N.; López-montes, A. M.; Ballesta-claver, J.; Collado-montero, F. J.; Blanc garcía, M. D. R. Identification of Indigo Dye (Indigofera Tinctoria) and Its Degradation Products by Separation and Spectroscopic Techniques on Historic Documents and Textile Fibers. *Stud. Conserv.* **2021**, *66* (1), 7−22.
(77) Christie, R. M. Why Is Indigo Blue? *Biotechnol. Histochem.* **2007**, *82* (2), 51−56.
(78) Acelas, M.; Castellanos, N. J.; Sierra, C. A. Stability and Performance Enhancement of an Oligo (Phenylene Vinylene) Photocatalyst via Surface Grafting onto TiO_2 for Visible-Light Indigo Carmine Degradation. *ChemistrySelect* **2022**, *7* (9), No. e202103460.
(79) Zhou, X.; Guo, Y.; Shi, L.; Han, Q.; Lin, C.; Zhang, L.; Wu, M.; Zhang, W. Degradation Pathways and Mechanisms Insight of Indigo and Shikonin with Experiments and Quantum Chemical Calculations. *Dye. Pigment.* **2023**, *218*, 111455.
(80) Zhang, X.; Foote, C. S.; Khan, S. I. Reactions of N-Acylated Indoles with Singlet Oxygen. *J. Org. Chem.* **1993**, *58* (1), 47−51.
(81) Kuramoto, N.; Kitao, T. Contribution of Singlet Oxygen to the Photofading of Indigo. *J. Soc. Dye. Colour.* **1979**, *95* (7), 257−261.
(82) Chiu, Y. H.; Chang, T. F. M.; Chen, C. Y.; Sone, M.; Hsu, Y. J. Mechanistic Insights into Photodegradation of Organic Dyes Using Heterostructure Photocatalysts. *Catalysts* **2019**, *9* (5), 430.
(83) Serrano-andrés, L.; Roos, B. O. A Theoretical Study of the Indigoid Dyes and Their Chromophore. *Chem. - A Eur. J.* **1997**, *3* (5), 717−725.
(84) Huerta-flores, A. M.; Torres-martínez, L. M.; Moctezuma, E.; Singh, A. P.; Wickman, B. Green Synthesis of Earth-Abundant Metal Sulfides (FeS_2, CuS, and NiS_2) and Their Use as Visible-Light Active Photocatalysts for H_2 Generation and Dye Removal. *J. Mater. Sci. Mater. Electron.* **2018**, *29* (13), 11613−11626.
(85) Neto, J. S. G.; Satyro, S.; Saggioro, E. M.; Dezotti, M. Investigation of Mechanism and Kinetics in the TiO_2 Photocatalytic Degradation of Indigo Carmine Dye Using Radical Scavengers. *Int. J. Environ. Sci. Technol.* **2021**, *18* (1), 163−172.
(86) Toghan, A.; Abd el-lateef, H. M.; Taha, K. K.; Modwi, A. Mesoporous TiO_2@g-C_3N_4 Composite: Construction, Characterization, and Boosting Indigo Carmine Dye Destruction. *Diam. Relat. Mater.* **2021**, *118*, 108491.
(87) Krieger, W.; Lamsfuß, J.; Zhang, W.; Kockmann, N. Local Mass Transfer Phenomena and Chemical Selectivity of Gas-Liquid Reactions in Capillaries. *Chem. Eng. Technol.* **2017**, *40* (11), 2134−2143.
(88) Lee, Y.; Von gunten, U. Oxidative Transformation of Micropollutants during Municipal Wastewater Treatment: Comparison of Kinetic Aspects of Selective (Chlorine, Chlorine Dioxide, Ferrate^{VI}, and Ozone) and Non-Selective Oxidants (Hydroxyl Radical). *Water Res.* **2010**, *44* (2), 555−566.
(89) Wang, Y.; Lin, Y.; He, S.; Wu, S.; Yang, C. Singlet Oxygen: Properties, Generation, Detection, and Environmental Applications. *J. Hazard. Mater.* **2024**, *461*, 132538.

https://doi.org/10.1021/acs.jpcc.3c08165
J. Phys. Chem. C 2024, 128, 5011−5029